Biomass-burning-derived particles from a wide variety of fuels: Part 2: Effects of photochemical aging on particle optical and chemical properties

Christopher D. Cappa[1,2,*], Christopher Y. Lim[3], David H. Hagan[3], Matthew Coggon[4,5,7], Abigail Koss[4,5,^], Kanako Sekimoto[4,5,6], Joost de Gouw[5,7], Timothy B. Onasch[8], Carsten Warneke,[4,5] Jesse H. Kroll[3]

[1] Department of Civil and Environmental Engineering, University of California, Davis, CA, USA 95616

[2] Atmospheric Sciences Graduate Group, University of California, Davis, CA, USA 95616

[3] Department of Civil and Environmental Engineering, Massachusetts Institute of Technology, Cambridge, MA, USA

[4] NOAA Earth System Research Laboratory (ESRL), Chemical Sciences Division, Boulder, CO 80305, USA

[5] Cooperative Institute for Research in Environmental Sciences, University of Colorado Boulder, Boulder, CO 80309, USA

[6] Graduate School of Nanobioscience, Yokohama City University, Yokohama, Kanagawa 236-0027, Japan

[7] Department of Chemistry, University of Colorado Boulder, Boulder, CO 80302, USA

[8] Aerodyne Research, Billerica, MA 01821, USA

[^] Now at Department of Civil and Environmental Engineering, Massachusetts Institute of Technology, Cambridge, MA, USA

[*] To whom correspondence should be addressed: cdcappa@ucdavis.edu

KEY POINTS

- Despite wide diversity in properties of primary particles produced from biomass combustion, photochemical aging engenders generally consistent changes

- Photochemical aging alters the absorptivity of brown carbon (aka absorbing organic aerosol) resulting from secondary organic aerosol production and heterogeneous oxidation

30

31 **ABSTRACT**

32 Particles in smoke emitted from biomass combustion have a large impact on global climate

33 and urban air quality. There is limited understanding of how particle optical properties—especially

34 the contributions of black carbon (BC) and brown carbon (BrC)—evolve with photochemical

35 aging of smoke. We analyze the evolution of the optical properties and chemical composition of

36 particles produced from combustion of a wide variety of biomass fuels, largely from the Western

37 U.S.. The smoke is photochemically aged in a reaction chamber over atmospheric-equivalent

38 timescales ranging from 0.25-8 days. Various aerosol optical properties (e.g., the single scatter

39 albedo, the wavelength dependence of absorption, and the BC mass absorption coefficient

40 (MAC_{BC})) evolved with photochemical aging, with the specific evolution dependent on the initial

41 particle properties and conditions. The impact of coatings on BC absorption (the so-called lensing

42 effect) was small, even after photochemical aging. The initial evolution of the BrC absorptivity

43 (MAC_{BrC}) varied between individual burns, but decreased consistently at longer aging times; the

44 wavelength-dependence of the BrC absorption generally increased with aging. The observed

45 changes to BrC properties result from a combination of SOA production and heterogeneous

46 oxidation of primary and secondary OA mass, with SOA production being the major driver of the

47 changes. The SOA properties varied with time, reflecting both formation from precursors having

48 a range of lifetimes with respect to OH and the evolving photochemical environment within the

49 chamber. Although the absorptivity of BrC generally decreases with aging, the dilution-corrected

50 absorption may actually increase from the production of SOA. These experimental results provide

51 context for the interpretation of ambient observations of the evolution of particle optical properties

52 in biomass combustion-derived smoke plumes.

53

54 **PLAIN LANGUAGE SUMMARY**

55 Particles and gases from combustion of a wide range of biomass fuels (e.g. leaves, twigs, logs,

56 peat, dung) were continuously photochemically aged in a small chamber up to eight days of

57 equivalent atmospheric aging. The properties of the emitted particles and smoke depended on the

58 fuel used and the combustion conditions. Upon aging, the particle chemical composition and

59 ability to absorb sunlight changed as a result of conversion of gases into particulate material and

60   from conversion of emitted particulate material into a different chemical form. We developed a

61   model to explain the observations, and used this to derive insights into the aging of smoke in the

62   atmosphere.

63

64   **KEYWORDS**

65   0305 Aerosols and particles; 0325 Evolution of the atmosphere; 0345 Pollution: urban and

66   regional; 0360 Radiation: transmission and scattering

67   **1   Introduction**

68   Open and contained biomass combustion contributes substantial amounts of particular matter

69   to the atmosphere (Bond et al., 2004). The emitted particles have a strong influence on global

70   climate by scattering and absorbing solar radiation and impacting cloud properties and

71   stratospheric water content (Penner et al., 1992;Sherwood, 2002;Jacobson, 2014). Biomass

72   burning-derived particles (BB particles, for short) also have substantial negative impacts on human

73   health globally (Lelieveld et al., 2015), especially when produced as a result of indoor combustion

74   associated with residential cooking and heating. In some parts of the world the frequency and

75   severity of uncontrolled fires is rising and projected to become worse in the future as a consequence

76   of climate change (Dale et al., 2001;Stephens et al., 2013) with effects already being seen in some

77   regions (McClure and Jaffe, 2018).

78   Particles produced from biomass burning are primarily composed of organic material and black

79   carbon (Andreae and Merlet, 2001). The relative contribution of organic aerosol (OA) and black

80   carbon (BC) depends on the burn conditions, which is strongly related to the fuel type and other

81   environmental factors (McMeeking et al., 2009;McClure et al., 2019). The chemical, optical, and

82   physical properties of freshly emitted BB particles produced from burning of various biomass fuel

83   types under various conditions are reasonably well studied (e.g. Lewis et al., 2008;McMeeking et

84   al., 2009;Levin et al., 2010;Cheng et al., 2016;Fortner et al., 2018;McClure et al., 2019). Such

85   measurements have established that some fraction of the emitted OA is light absorbing, with the

86   absorptivity dependent upon on the burn conditions (Saleh et al., 2014). Light absorbing OA is

87   commonly referred to as brown carbon (BrC). Compared to BC, brown carbon is generally less

88   absorbing and exhibits a much stronger wavelength dependence (Kirchstetter et al., 2004;Andreae

3

89   and Gelencser, 2006). As such, the importance of BrC to light absorption tends to increase as

90   wavelength decreases.

91   The influence of atmospheric processing on the properties of biomass combustion smoke has

92   received less attention, especially in the context of how aging influences BB particle optical

93   properties. (Here, we use "smoke" to indicate the mixture of particles and gases emitted from

94   biomass combustion.) Understanding how BB particles evolve over time is key to establishing

95   their atmospheric impacts (Feng et al., 2013;Wang et al., 2014;Wang et al., 2018). Field

96   observations of the effects of photochemical aging on BB particle optical properties, and in

97   particular light absorption, are sparse. Forrister et al. (2015) observed that absolute absorption by

98   water soluble BrC decreased over time within a biomass-burning plume, with a decay time

99   constant of about a day. Wang et al. (2016) observed that the BrC absorptivity (as opposed to the

100 absolute absorption) decreased with photochemical age, with a similar time constant as reported

101 by Forrister et al. (2015). However, both studies suggest that there is some fraction of the BrC that

102 is more persistent and less subject to photochemical degradation, and Zhang et al. (2017) found no

103 decrease in BrC absorption with age for particles in convective outflow. Laboratory measurements

104 can help provide mechanistic understanding necessary to comprehensively interpret the field

105 observations. Most laboratory studies investigating photochemical aging effects on optical

106 properties, and in particular light absorption, of BB particles have done so for only a small number

107 of individual fuel types or burn conditions and often for particles alone rather than smoke (e.g.,

108 Saleh et al., 2013;Sumlin et al., 2017;Tasoglou et al., 2017;Wong et al., 2017;Kumar et al., 2018).

109 Thus, while these studies have proven insightful, the limited number of fuels and conditions

110 considered makes extending the observations to the atmosphere thus far challenging.

111   In this study, we examine how the optical properties of BB particles evolve as a result of OH

112 radical dominated photochemical aging for smoke derived from combustion of a multitude of fuel

113 types and spanning a wide range of burn conditions. We characterize the influence of

114 photochemical aging on optical properties for a substantially greater number of fuel types than

115 have been reported previously in the literature, for burn conditions ranging from mostly flaming

116 to entirely smoldering. We access aging time scales ranging from a fraction of a day to many days

117 and characterize the continuous evolution of the particle properties. We show that the BB particle

118 optical properties evolve with photochemical oxidation, linked both to chemical evolution of the

119 primary particles and production of secondary organic aerosol. We characterize and quantify this

4

120 behavior, developing a generalizable model for the evolution of brown carbon properties in
121 wildfire plumes.

2 Methods

2.1 Campaign overview and sampling strategy

124   The Fire Influence on Regional to Global Environments and Air Quality Experiment (FIREX-
125 AQ) lab campaign took place at the Missoula Fire Sciences Laboratory in November 2016
126 (NOAA, 2013). A full description of the sampling strategy and methods, including descriptions of
127 instruments used, for our study is provided in Lim et al. (2019) and McClure et al. (2019). Only a
128 short description is provided here. A wide-variety of fuels (**Table S1**) were combusted under
129 realistic conditions in a large combustion chamber (ca. 12 m x 12 m x 19 m). Fuels included bear
130 grass, rice straw, chaparral (chamise and manzanita), juniper, sagebrush, canopy, litter and mixed
131 components from hard woods (fir, pine, spruce), rotten logs, peat, dung. Data from the FIREX lab
132 study are available via the NOAA website (https://www.esrl.noaa.gov/csd/projects/firex/firelab/;
133 last access date 24 January 2020), with data specific to this work also archived as Cappa et al.
134 (2019a).

135   The particle and gas emissions from individual burns were injected into a 0.15 m^3
136 photochemical reaction chamber (the "mini chamber"). A burn typically lasted about 10-20
137 minutes. Smoke was transferred from the burn room to the adjacent room housing the mini
138 chamber and associated instrumentation through a 30 m long high-velocity community inlet. The
139 residence time in the community inlet was determined as <2 s. Smoke from the community inlet
140 was sub-sampled into the mini chamber through a PM$_1$ cyclone using an ejector diluter. There
141 were some losses of particles and gases during transfer. However, comparison between the VOC
142 concentrations measured prior to sampling through the community inlet and from the mini
143 chamber prior to photooxidation demonstrate losses were relatively minor (<8% per volatility bin,
144 across the entire measured VOC distribution) and should not substantially impact the results here
145 (Coggon et al., 2019;Lim et al., 2019).

5

146 **2.2 The mini chamber**

147   Prior to each burn, the chamber was flushed with clean air with RH ranging from 25-40%.

148 Smoke was sampled into the mini chamber across an entire burn or until shortly after the

149 concentration in the mini chamber reached maximum. An instruments suite continuously sampled

150 air from the mini chamber (see below). Clean make-up air added from a zero-air generator

151 (Teledyne 701H) ensured the total inflow (sample + make-up air) equaled the air being sampled

152 out of the chamber. The actual flowrate out of the chamber varied slightly between experiments

153 dependent upon the exact instrument suite. Given the mini chamber volume and the typical

154 flowrates, the net dilution from the community inlet was about a factor of seven.

155   Details of the mini chamber and its operation are provided in Lim et al. (2019). The FIREX

156 mini chamber operated in semi-batch mode, where unoxidized smoke-laden air is first sampled

157 into the mini chamber. After the sampling period, a clean airflow replaces the sample flow,

158 maintaining the size of the bag over time. Oxidation is initiated by turning on one 254 nm UV

159 light. Externally generated ozone added at 50-100 ppb serves to initiate production of OH radicals

160 via generation of $O(^1D)$. The concentrations of gases and particles continuously decreased owing

161 to dilution by clean air and wall losses. The observed decay rate of acetonitrile (ACN) provides

162 the dilution rate (see Section 2.3). The ACN loss rate, characterized as $-d\log[ACN]/dt$, was around

163 0.024 min^{-1}, consistent with the gas flow rates. The particle loss rate was greater owing to

164 additional losses of particles to the walls of the chamber. The general particle mass loss rate was

165 $-d\log[particles]/dt \sim 0.038$ min^{-1}. However, for BC-rich particles the loss rate was initially

166 enhanced when the lights were turned on, discussed further below. OH exposures were determined

167 from the dilution-corrected decay of deuterated n-butanol (D9). These are converted to an

168 equivalent time-evolving photochemical age (t_{OH}) assuming $[OH] = 1.5 \times 10^6$ molecules cm^{-3}. The

169 t_{OH} ranged from 0.25 to about 8 days of equivalent aging. The n-butanol (D9) measurements were

170 available for only about half of the individual burn experiments owing to data availability

171 limitations of the VOC measurements. While there is some experiment-to-experiment variability

172 in the t_{OH} values accessed, the relationship between experiment time and t_{OH} is reasonably

173 consistent. Thus, we use the average behavior to estimate the photochemical ages for experiments

174 lacking direct measurement.

Atmospheric
Chemistry
and Physics
Discussions

175   As discussed in Coggon et al. (2019), the conditions of the mini chamber do not perfectly

176   represent the photochemical conditions of the atmosphere. The use of the 254 nm UV lights

177   enhances photolysis of a small number of select non-methane organic gases (NMOG), especially

178   furfural. In contrast, photolysis of NO_2 is likely substantially slower than in the atmosphere. This

179   impacts the time-evolution of the NO/NO_2 ratio, and consequently radical reactions (e.g. RO_2 +

180   NO) and NO_x loss processes. The influence of photobleaching of BrC is likely underestimated

181   relative to the atmosphere as the actual exposure time (tens of minutes) is much shorter than the

182   equivalent photochemical age (many days). Overall, the photochemical environment in the mini

183   chamber emphasizes OH-driven oxidation under initially high-NO_x conditions that rapidly shift

184   towards low-NO_x conditions (Coggon et al., 2019).

185   **2.3   Instrumentation**

186   The suite of instruments sampling from the mini chamber are listed in **Table S2** and further

187   details of instrument operation and uncertainties are provided in McClure et al. (2019), Lim et al.

188   (2019), and Coggon et al. (2019). In brief, particle-phase instruments sampled alternatingly

189   through a two-stage thermodenuder that operated at 150°C and 250 °C with a residence time of ~5

190   seconds. The cycle rate between ambient and thermodenuder sampling was 2 minutes. The ambient

191   ("bypass") line on the thermodenuder was lined with charcoal cloth to remove excess NMOG, O_3,

192   and NO_2 that might otherwise interfere with the measurements. Particle size distributions were

193   measured using a scanning electrical mobility spectrometer (SEMS; Model 2002, Brechtel Mfg.,

194   Inc.). The overall concentration and composition of sub-micron non-refractory particulate matter

195   (NR-PM_1) were measured using a high-resolution time-of-flight aerosol mass spectrometer (HR-

196   AMS; Aerodyne Research, Inc.). The concentration and composition of refractory BC-containing

197   particles was characterized using a soot particle aerosol mass spectrometer (SP-AMS; Aerodyne

198   Research, Inc.); the SP-AMS was operated with only laser-vaporization of particles such that it

199   was sensitive to only those particles containing refractory black carbon (rBC). Refractory black

200   carbon concentrations and size distributions for volume-equivalent diameters from 90-350 nm

201   were quantitatively measured using a single particle soot photometer (SP2; DMT). Refractory BC

202   outside of this size window was accounted for through multi-modal fitting of the observed mass-

203   weighted size distributions. Gas-phase instruments sampled directly from the mini chamber

204   through Teflon sampling lines. These included: a proton-transfer-reaction time-of-flight mass

205   spectrometer (PTR-ToF-MS) to characterize primary organic gases (Yuan et al., 2017); an

206   I$^-$ chemical ionization mass spectrometer to characterize various gas-phase organic oxidation

207   products; an ozone monitor (2B Technologies, Model 202); a CO monitor (Teledyne, Model

208   T300), and a CO_2 monitor (LI-COR, LI-840A).

209   **2.4   Brown carbon, coatings, and particle classification**

210   Mass absorption coefficients, referenced to BC, are calculated as:

211    $$MAC_{BC} = \frac{b_{abs}}{[BC]};$$ (1.)

212   where b_{abs} is the absorption coefficient (Mm^{-1}) and [BC] is the concentration of refractory black

213   carbon (µg m^{-3}). The observed MAC_{BC} may include contributions to absorption from both the BrC

214   (the BrC enhancement, $E_{abs,BrC}$) and from the so-called lensing effect that can occur when non-

215   absorbing coatings mix with BC (the coating-induced enhancement, $E_{abs,coat}$) (Cappa et al.,

216   2012;Lack et al., 2012). The observable absorption enhancement is characterized as:

217    $$E_{abs} = \frac{MAC_{BC,obs}}{MAC_{BC,ref}};$$ (2.)

218   where $MAC_{BC,obs}$ is the observed value and $MAC_{BC,pure}$ is a reference value for pure, uncoated BC.

219   The reference $MAC_{BC,pure}$ can be established from the literature or from the observations; we take

220   the latter approach here, using wavelength-specific $MAC_{BC,pure}$ values determined by McClure et

221   al. (2019) for this data set. The $MAC_{BC,pure}$ = 11.8 m^2 g^{-1} (405 nm), 8.8 m^2 g^{-1} (532 nm) and 5.5 m^2

222   g^{-1} (781 nm). The use of a campaign-specific value helps to mitigate instrumental uncertainties in

223   determining E_{abs} (Cappa et al., 2019b).

224   The $E_{abs,781nm}$ observed for primary particles was near unity with a negligible dependence on

225   the coating-to-BC mass ratio ($R_{coat-rBC}$) (McClure et al., 2019). We observe limited change in the

226    $E_{abs,781nm}$ with photochemical aging here, with $E_{abs,781nm}$ for aged particles averaging 1.19 for

227    $R_{coat-rBC}$ < 9 (**Figure S2**). The $MAC_{BC,781nm}$ only increases notably (by more than 10%) when

228    $R_{coat-rBC}$ > 9, well above where theory predicts the $MAC_{BC,781nm}$ should increase by a substantial

229   amount (Fuller et al., 1999). Other laboratory experiments, often performed using mono-disperse

230   BC seed particles, have observed substantial coating-induced enhancements and a dependence on

231   the $R_{coat-rBC}$ (e.g. Cross et al., 2010;Shiraiwa et al., 2010;Cappa et al., 2012;Metcalf et al.,

232   2013;Peng et al., 2016a;You et al., 2016). We suggest that the small $E_{abs,coat}$ for photochemically

233   aged biomass combustion particles results from three phenomena: (i) condensation occurring onto

234   a polydisperse rBC distribution, leading to some particles having very thick coatings and some

235   quite thin, yielding a large average $R_{coat-rBC}$ yet small enhancement (Fierce et al., 2016;Fierce et

236   al., Accepted); (ii) the coated biomass burning-derived rBC particles not having a core-shell

237   morphology and reduced $E_{abs,coat}$ (Helgestad, 2016;Liu et al., 2017); and, (iii) weak absorption by

238   BrC at 781 nm by both internally and externally mixed BrC that becomes notable only when the

239   total [OA] greatly exceeds [BC] (McClure et al., 2019). This is supported by the comparably much

240   stronger relationship for photochemically aged particles between $MAC_{BC,781nm}$ and the [OA]/[rBC]

241   ratio than with the $R_{coat-rBC}$ (**Figure S2**). This suggests that the majority of the variability in the

242     $MAC_{BC,781nm}$ derives from varying contributions of BrC, rather than in $E_{abs,coat}$, and that $E_{abs,coat}$ is

243   near unity.

244   The wavelength-specific BrC absorption ($b_{abs,BrC}$) is estimated as:

245     $$b_{abs,BrC} = b_{abs,obs} - MAC_{BC,ref} \cdot [rBC] \cdot E_{abs,coat} \qquad (3.)$$

246   Given the above discussion and the complementary discussion in McClure et al. (2019), we assume

247     $E_{abs,coat}$ is unity, with the derived $b_{abs,BrC}$ an upper limit. A lower limit for $b_{abs,BrC}$ can be obtained

248   using an empirical $E_{abs,coat}$ versus $R_{BC-coat}$ relationship. For the aged particles, the average upper-

249   limit $b_{abs,BrC}$ values are 11(±9)% at 405 nm and 29(±16)% at 532 nm higher than the lower limit.

250   The uncertainties in $b_{abs,BrC}$ and the derived MAC_{BrC} scale inversely with the [OA]/[rBC] ratio,

251   where MAC_{BrC} is:

252     $$MAC_{BrC} = \frac{b_{abs,BrC}}{[OA]} \qquad (4.)$$

253   The MAC_{BrC} values are bulk-average values and do not account for different molecules and classes

254   of molecules likely having different absorptivities. Uncertainty in the estimated $MAC_{BC,pure}$ and

255   measured b_{abs}, and [rBC] also contribute to uncertainty in the estimated MAC_{BrC}.

256   The Ångström absorption exponent (AAE) characterizes the wavelength dependence of

257   absorption:

258     $$AAE_{\lambda 1-\lambda 2} = -\log\left(\frac{b_{abs,\lambda_1}}{b_{abs,\lambda_2}}\right) / \log\left(\frac{\lambda_1}{\lambda_2}\right); \qquad (5.)$$

Atmospheric
Chemistry
and Physics
Discussions
Open Access
EGU

259   where λ_1 and λ_2 indicate two different measurement wavelengths. The AAE can be calculated

260   based on the total absorption or just for BrC, with the latter designated as AAE_{BrC}. The single-

261   scatter albedo (SSA) characterizes the fraction of light extinction attributable to scattering:

262    $$SSA_\lambda = \frac{b_{ext} - b_{abs}}{b_{ext}} = \frac{b_{sca}}{b_{ext}}$$ (6.)

263   McClure et al. (2019) classified individual experiments into six classes dependent on the primary

264   particles SSA_{405nm}. We use these same classifications, ranging from class 1—primary particles

265   having low SSA_{405nm} values (0.22 - 0.38) and small [OA]/[rBC] (0.3 - 2.6)—to class 6—primary

266   particles having high SSA_{405nm} values (0.94 to 0.96) and very large [OA]/[rBC] (400 to 1 x 10^5)—

267   to interpret the influence of photochemical aging. **Table S3** provides the general relationship

268   between fuel type, SSA, and log([OA]/[BC]). As noted by McClure et al. (2019), the classifications

269   relate somewhat to the burn-average modified combustion efficiency (MCE), which characterizes

270   the burn efficiency, with class 1 generally deriving from more efficient, flaming burns having

271   higher MCE and class 6 from more less efficient, smoldering burns having lower MCE. The

272   average dependence of the various aerosol properties on photochemical age is determined for each

273   SSA class. Grouping experiments by SSA classification is justified given the substantial variability

274   in the primary particle properties between individual burns. The focus on average behavior

275   increases robustness of the resulting interpretation as sensitivity to experiment-by-experiment

276   differences (e.g., length of experiment, initial concentration, amount of fuel consumed) is reduced.

277   **3   Results and Discussion**

278   **3.1   Observations of the influence of photochemical aging on optical properties**

279   3.1.1 Total particles (black + brown carbon)

280   The suite of intensive optical (e.g. SSA, MAC, AAE) and chemical and physical properties (e.g.

281   [OA]/[rBC], $R_{coat-rBC}$) vary with photochemical aging; the average behavior for each particle class

282   is shown in **Figure 1** and the experiment-specific behavior within each class in **Figure S3** through

283   **Figure S8**. The majority of the mass formed is OA, with minor contributions from inorganic

284   species. A detailed assessment of SOA formation is provided by Lim et al. (2019).

285   The changes observed for the lower number (more BC-rich) particle classes are typically more

286   pronounced than for the higher number (more OA-rich) particle classes. For example, the class 1

Atmospheric
Chemistry
and Physics
Discussions

Open Access

EGU

287   SSA_{405nm} increases from 0.3 to 0.7 and the $AAE_{405-532}$ from 1.4 to 3.5 with aging, while the class

288   6 SSA_{405nm} remains near constant at 0.94 and the $AAE_{405-532}$ decreases slightly from ca. 7 to 5.

289   Notably, the $AAE_{405-532}$ converge towards a common value, around 4, with aging. While there

290   remain some class specific differences, this indicates that the SOA that is forming has similar

291   optical properties independent of the initial burn conditions.

292   Also, the [OA]/[BC] for class 1 increases by a factor of nearly 70 while the increase for class

293   6 is ten times smaller, and the particle class 1 $R_{coat-rBC}$ increases by a factor of 11 while there is

294   negligible change for particle class 6. Generally, the most rapid changes occur when the equivalent

295   aging time is less than a day, with slower changes after this. Some of the observed changes, in

296   particular for class 1 and class 2 particles, results from enhanced loss of BC-rich particles when

297   the lights are turned on, although this alone cannot explain the differing extents of change and

298   would not directly impact the $R_{coat-rBC}$ (Section 3.2.1). These observations indicate substantial

299   formation of secondary OA and a net increase in the overall (dilution-corrected) OA, consistent

300   with Lim et al. (2019). If secondary OA formation were offset by evaporation of primary OA then

301   the SSA would not have increased, nor would the [OA]/[rBC] or $R_{coat-rBC}$ ratios have increased.

302   Additionally, the OA O:C atomic ratio increases and the AMS f_{60} (a marker for primary

303   biomass burning OA attributed to levoglucosan and similar species) decreases rapidly with

304   photochemical aging (**Figure 1**). However, unlike the above properties, the O:C and f_{60} evolution

305   are generally similar between SSA classes, despite some variability in the primary particle

306   properties (McClure et al., 2019). The changes in both O:C and f_{60} occur more rapidly than can be

307   explained by heterogeneous oxidation, implying rapid photochemical production of secondary OA

308   (Lim et al., 2019). The O:C increases rapidly at $t_{OH} < 1$ day with continual increases with further

309   aging . The f_{60} values decline rapidly at $t_{OH} < 1$ day to around $f_{60} = 0.008$, changing negligibly with

310   continued aging. It is noteworthy that the f_{60} plateaus around 0.008 upon aging, rather than at

311   0.003, the value denoted by Cubison et al. (2011) as the nominal background outside of biomass

312   burning influenced areas. This suggests that observation of f_{60} values much smaller than 0.008 in

313   ambient measurements indicate an influence of OA from non-biomass combustion sources (both

314   POA + SOA).

3.1.2 Brown Carbon

315

316   **Observations:** The class-average $MAC_{BrC,405}$ and the $AAE_{BrC,405-532}$ evolve with photochemical

317 aging (**Figure 2)**. Results for individual experiments are shown in **Figure S9** and **Figure S10**.

318 Overall, the $MAC_{BrC,405}$ values decrease from the primary values with aging. However, for the

319 initially less absorbing BrC, corresponding to the higher SSA classes (i.e., class 5 and 6), the

320 $MAC_{BrC,405}$ first increase at $t_{OH} < 1$ day before decreasing. This behavior suggests rapid formation

321 of SOA more absorbing than the primary OA for these classes, with production of less absorbing

322 SOA or conversion of POA or SOA via heterogeneous oxidation into less absorbing forms at later

323 times (discussed further in Section 3.2.2). The $MAC_{BrC,532}$ behave similarly (**Figure S11**). The

324 class-average $MAC_{BrC,405}$ values all converge around 0.2 m^2 g^{-1} after many days (~5) of equivalent

325 aging. The class-average $AAE_{BrC,405-532}$ converge towards $AAE_{BrC,405-532} \sim 5$ after many days of

326 equivalent aging, with the exact behavior dependent on the initial $AAE_{BrC,405-532}$.

327   **Comparison with literature:** Our observations can be compared with various literature

328 observations, where we use reported SSA or AAE values to infer the equivalent particle class

329 (**Table S4**). Martinsson et al. (2015) observed that the 370 nm OA absorptivity of class 1 particles

330 decreased after rapidly aging for $t_{OH} = 8.3$ days. Saleh et al. (2013) reported the AAE for class 1

331 particles produced from oak combustion changed negligibly (1.38 to 1.42) while the AAE for

332 particles from pine combustion increased slightly (1.48 to 1.73) after photochemically aging

333 smoke for t_{OH} of a few hours; the extent of aging was likely greater for the pine than oak. The AAE

334 for class 1 particles during FIREX increased to a greater extent (1.4 to 2.2) after similar aging (t_{OH}

335 ~ 6 h). Saleh et al. (2013) also report smaller SOA absorptivity compared to POA at 550 nm,

336 qualitatively consistent with our observations. Zhong and Jang (2014a) observed the 550 nm

337 absorptivity of class 5 particles initially increased over ~2 h, but then gradually declined upon

338 photochemical aging of smoke from smoldering combustion. This general behavior is consistent

339 with the behavior of the class 5 and 6 particles here, for which the MAC_{BrC} increased slightly in

340 the first few hours of equivalent aging followed by a continuous decline.

341   Similar to our observations, Kumar et al. (2018) observed $AAE_{370-660}$ values for class 1

342 particles increased from around 1.4 to 2 for photochemically aged beechwood smoke over $t_{OH} \sim 1$

343 day. They report that the primary OA is more absorbing than the SOA formed. We interpolate their

344 results to estimate MAC_{405} values for BC (12.4 m^2 g^{-1} ± 1.1), primary BrC (4.0 m^2 g^{-1} ± 1.3), and

Atmospheric
Chemistry
and Physics
Discussions

Open Access

EGU

345   secondary BrC (1.6 m^2 g^{-1} ± 1.4). The $MAC_{BC,405}$ value agrees well with our estimate of 11.8 m^2

346   g^{-1}. However, their primary $MAC_{BrC,405}$ substantially exceeds our class 1 average (2.25 m^2 g^{-1} ±

347   1.0) as does their primary BrC AAE (4.6 versus 2.2 ± 1.1, respectively), while their AAE for SOA

348   is similar to that observed here at longer aging times (5.5 versus ~5, respectively). Over their ~1

349   day of equivalent aging they find little variability in the MAC_{BrC} for SOA. Cappa et al. (2019b)

350   reported $MAC_{BrC,405}$ and $AAE_{405-532}$ for relatively fresh biomass burning derived organic aerosol in

351   the ambient atmosphere, reporting values (0.84 m^2 g^{-1} and 3.02, respectively) similar to those for

352   class 2 particles here.

353   Sumlin et al. (2017) heterogeneously aged class 6 particles with OH and observed negligible

354   changes in the absorptivity and SSA_{405} at 1 and 3.5 days of equivalent aging, but then a sudden

355   change at 4.5 days of equivalent aging. This differs substantially from our observations, where

356   changes occurred continuously; the reasons for this difference are unclear, although a

357   discontinuous change with increasing exposure is unexpected. Browne et al. (2019) also

358   heterogeneously aged class 6 particles with OH, but observed a continuous decrease in the

359   absorptivity with OH oxidation, consistent with the long-time behavior observed here. Wong et al.

360   (2017) photolytically aged (at 300-400 nm) water-soluble and water-insoluble solution extracts of

361   particles from smoldering combustion and observed that the particle absorptivity initially increased

362   over the course of about a day, peaked, and then declined over longer times to below the initial

363   value. While this general behavior is consistent with the evolution of our class 5 and 6 particles,

364   the photon flux here was likely too low for direct photolytic aging to contribute substantially (Peng

365   et al., 2016b), especially given the short absolute aging timescale in the mini chamber (tens of

366   minutes). Lee et al. (2014) photolytically aged water-soluble extracts of secondary BrC produced

367   from photooxidation of naphthalene and observed a continuous decrease in the absorptivity, but

368   again with a time constant that was likely too long to have influenced our experiments. Fleming et

369   al. (2020) photolytically aged particles from 12 of the FIREX burns that were collected on Teflon

370   filters. They observed a wide diversity of equivalent lifetimes (referenced to the time-averaged

371   photon flux in Los Angeles, CA) for different BrC chromophores, some of which were quite short

372   (<1 day). However, the equivalent lifetime of the total absorption was >10 days for all samples,

373   and with a recalcitrant component making up ca. 30% of the total absorption.

374   Overall, our results combined with the literature indicate that differences in starting conditions

375   (i.e., particle class) are important to consider when comparing between different photochemical

13

Atmospheric
Chemistry
and Physics
Discussions

Open Access
EGU

376   aging experiments on biomass combustion-derived particles. Additionally, it is important consider

377   whether a given experiment is likely to favor one process over another, e.g., SOA formation,

378   heterogeneous oxidation, or photolysis.

379   **3.2   Understanding and modeling the photochemical evolution of smoke**

380   3.2.1 Chamber photochemical model description

381   **Overview:** We observe that a wide range of particle properties evolve as the smoke from all

382   SSA classes is photochemically aged. To facilitate interpretation, we have developed a simplified

383   model of photooxidation that accounts for SOA formation from oxidation of gas-phase species,

384   heterogeneous oxidation, differential losses of particle types and dilution in the mini chamber. We

385   aim to simulate the evolution of the brown carbon absorptivity (i.e., MAC_{BrC}), specifically, using

386   the initial primary particle properties, gas-phase species, and evolution of the [OA]/[rBC], O:C,

387   and AMS f_{60} as constraints or guides as to the reasonableness of the general model formulation.

388   Model parameters are constrained as possible by the observations or tuned to provide for good

389   agreement with the observations for all particle classes (**Table 1** and **Table 2**). Our modeling

390   approach complements the analysis of Lim et al. (2019), who show that the amount of SOA formed

391   is directly related to the total amount of precursor non-methane organic gases (NMOG) in the

392   chamber and that the effective SOA mass yield increases with aging. Here, we take a more

393   mechanistic approach to understanding SOA formation in these experiments and focus on the

394   influence of SOA formation on the observed optical properties. The model framework, constraints,

395   and assumptions are described below.

396   **Reactive gases:** Biomass burning releases a wide variety of NMOG (Koss et al.,

397   2018;Sekimoto et al., 2018; and references therein). Upon oxidation, these NMOG can form SOA.

398   In general, higher molecular weight NMOG have a higher propensity to form SOA (Cappa and

399   Wilson, 2012). We consider the suite of gas-phase compounds measured by PTR-ToF-MS (Koss

400   et al., 2018) having molecular weights greater than 50 amu as potential SOA precursor compounds.

401   (Consideration of all species measured, including those with MW < 50 amu does not change the

402   results, consistent with Lim et al. (2019).) These 107 identified gas-phase compounds have been

403   binned according to their OH reaction rate coefficients reported by Koss et al. (2018) (**Figure S12**

404   and **Figure S13**). The OH rate coefficients range from 3 x 10^{-10} cm^3 molecules^{-1} s^{-1} (for

405   sesquiterpenes) to 1.4×10^{-13} (for nitrobenzene); most compounds have k_{OH} values greater than 4

406    $\times 10^{-12}$ cm^3 molecules^{-1} s^{-1}. Based on these observations, we make a simplifying assumption that

407   there are three general classes of SOA precursor molecules: those that react fast ($3 \times 10^{-10} \geq k_{OH} >$

408   3×10^{-11}); those that react slowly ($3 \times 10^{-11} \geq k_{OH} \geq 2 \times 10^{-12}$); and those that react very slowly (k_{OH}

409    $< 2 \times 10^{-12}$). The corresponding SOA type-specific k_{OH} values we use in the model are: $k_{OH,fast} = 4$

410    $\times 10^{-11}$ cm^3 molecules^{-1} s^{-1} ($\tau_{OH,fast} = 0.19$ days), $k_{OH,slow} = 9 \times 10^{-12}$ cm^3 molecules^{-1} s^{-1} ($\tau_{OH,slow} =$

411   0.86 days), and $k_{OH,VS} = 7 \times 10^{-13}$ cm^3 molecules^{-1} s^{-1} ($\tau_{OH,VS} = 11$ days) (**Table 1** and **Figure S12**).

412   (The time constants given correspond to $[OH] = 1.5 \times 10^6$ molecules cm^{-3}.) The dividing lines

413   between the NMOG classes are somewhat arbitrary, but capture the general overall behavior and

414   are consistent with variable observed formation timescales of secondary NMOG (Coggon et al.,

415   2019). Loss of primary species due to photolysis is not considered; Coggon et al. (2019) show that

416   rapid photolysis dominates loss for a small number of primary species, notably furfural. These

417   species tend to be fast reacting, and thus are incorporated in the fast NMOG group, although their

418   actual loss rate is likely underestimated.

419   The initial total NMOG concentration is specified relative to the initial [OA], consistent with

420   Lim et al. (2019). The observed average ratio between the total carbon mass concentration

421   measured by the PTR-ToF-MS and the initial [OA] carbon mass is 7 ± 3. SSA class-specific initial

422   [NMOG]/[OA] values are specified in the model, constrained to fall around this range (**Table 2**).

423   This initial gas-phase mass is apportioned between the fast, slow, and very slow NMOG. The PTR-

424   TOF-MS measurements indicate that the relative abundances of fast, slow, and very slow reacting

425   NMOG average approximately 0.5:0.4:0.1 on a mass basis. We specify the very slow NMOG

426   fraction as a constant and allow the relative abundances of fast and slow reacting NMOG to vary

427   between the particle classes, with specific values determined from fitting to the observations; the

428   derived values are in general agreement with the observed range (**Table 2**). Allowing for some

429   variability is reasonable, given that the NMOG composition varied between experiments and with
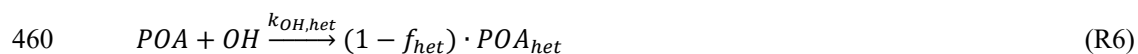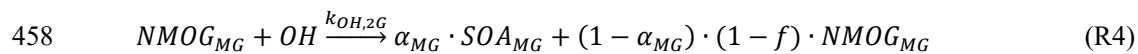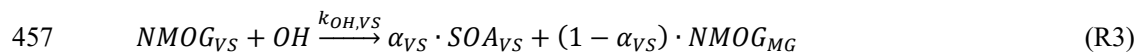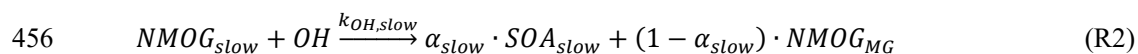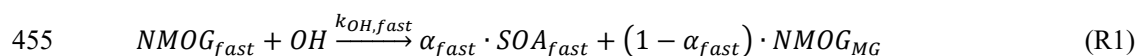
430   burn type (Sekimoto et al., 2018).

431   The influence of multi-generation chemistry is accounted for by assuming all gas-phase

432   products from reaction of primary precursors are reactive towards OH radicals. This multi-

433   generational (MG) chemistry is simplified by assuming that all MG species react identically,

434   independent of the actual generation number (i.e., number of times reacted) or precursor identity.

435 This allows for a substantial reduction in the number of species tracked relative to more explicit

436 methods (Aumont et al., 2005;Cappa and Wilson, 2012).The assumed multi-generational oxidation

437 OH reaction rate coefficient, $k_{OH,MG}$, is set to 5 x 10^{-12} cm^{-3} molecules^{-1} cm^{-1} ($\tau_{OH,MG}$ = 1.54 days).

438 The $k_{OH,MG}$ falls between the fast and slow species. MG species are assumed to fragment upon

439 reaction, with a fragmentation probability (f) of 15%, serving to limit the maximum SOA

440 formation; assuming a constant f is a simplification over more detailed approaches (Cappa and

441 Wilson, 2012).

442 **SOA formation and processing:** SOA forms upon reaction of the primary NMOG types and

443 MG species, referred to here as SOA$_{fast}$, SOA$_{slow}$, SOA$_{VS}$, and SOA$_{MG}$. SOA formation occurs here

444 with fixed yields (α) assuming both instantaneous and irreversible (i.e., non-volatile)

445 condensation, simplifications over more detailed approaches. The influence of vapor wall losses

446 (Zhang et al., 2014) is not explicitly considered, and thus reflected in the derived α values. SOA

447 and POA also react heterogeneously with OH, producing oxidized OA that can also react with OH.

448 We assume an OH reactive uptake coefficient (γ_{OH}) of unity for all OA types. Upon oxidation,

449 15% of the POA and SOA mass is assumed lost owing to fragmentation and volatilization of the

450 products (i.e., $f_{het,x}$ = 0.15). Heterogeneous oxidation of oxidized OA occurs leads only to

451 fragmentation reflecting the greater propensity for more oxidized species to fragment upon

452 reaction (Kroll et al., 2015). The $k_{OH,het}$ values are calculated using the [OH] with the observed

453 surface-weighted particle diameters and appropriate mass-transfer corrections (Smith et al., 2009).

454 The overall reaction scheme is summarized below:

455 $$NMOG_{fast} + OH \xrightarrow{k_{OH,fast}} \alpha_{fast} \cdot SOA_{fast} + (1 - \alpha_{fast}) \cdot NMOG_{MG} \tag{R1}$$

456 $$NMOG_{slow} + OH \xrightarrow{k_{OH,slow}} \alpha_{slow} \cdot SOA_{slow} + (1 - \alpha_{slow}) \cdot NMOG_{MG} \tag{R2}$$

457 $$NMOG_{VS} + OH \xrightarrow{k_{OH,VS}} \alpha_{VS} \cdot SOA_{VS} + (1 - \alpha_{VS}) \cdot NMOG_{MG} \tag{R3}$$

458 $$NMOG_{MG} + OH \xrightarrow{k_{OH,2G}} \alpha_{MG} \cdot SOA_{MG} + (1 - \alpha_{MG}) \cdot (1 - f) \cdot NMOG_{MG} \tag{R4}$$

459 $$SOA_i + OH \xrightarrow{k_{OH,het}} (1 - f_{het}) \cdot SOA_{het} \tag{R5}$$

460 $$POA + OH \xrightarrow{k_{OH,het}} (1 - f_{het}) \cdot POA_{het} \tag{R6}$$

16

461   SOA_{het} or $POA_{het} + OH \xrightarrow{k_{OH,het}} volatile\ products$ (R7)

462   Reactions 1-4 represent oxidation of gas-phase species and SOA formation. Reaction 5 represents

463   the heterogeneous oxidation of fast, slow, very slow or multi-generation SOA and conversion to

464   an oxidized SOA product, while Reaction 6 represents heterogeneous oxidation of POA to an

465   oxidized product. Reaction 7 indicates that reaction of oxidized OA only produces volatile

466   products.

467   **Dilution and particle wall losses:** Given the semi-batch operation method for the mini

468   chamber, the concentration of particles and gases all decreased over time owing to dilution and

469   losses to the chamber walls. The non-OH loss rate of gases was assumed constant in the model,

470   consistent with observations during an experiment where the lights were left off. However, we

471   observed that the overall decay of BC particles containing little coating material (e.g. class 1 and

472   class 2) was enhanced when the lights were turned on, while it was not for particles having thicker

473   initial coating amounts (**Figure S14** and **Figure S15**). This enhanced loss was unique to BB

474   particles, as no such behavior was observed for either atomized fullerene soot (highly absorbing)

475   or ammonium sulfate (non-absorbing). That enhanced decay occurs for the BC-rich particles

476   suggests that this phenomenon is related to the amount of coating material, since the class 1 and 2

477   particles have substantially smaller initial $R_{coat,rBC}$ values compared to the other classes (**Figure 1**

478   and McClure et al. (2019)). We speculate that the enhanced loss of BC-rich particles results from

479   their having a greater propensity towards photoelectric charging with the 254 nm light, as

480   photoelectric charging is highly sensitive to the state of the particle surface (Burtscher, 1992). We

481   determined an empirical relationship between the observed time-varying rBC decay rate and the

482   coating amount for use in the model (**Figure S16**). The decay rate slows as particles become more

483   coated (i.e., have larger $R_{coat,rBC}$), eventually reaching a plateau. We also account for the mixing

484   state of the particles when determining particle loss rates, as McClure et al. (2019) showed that the

485   fraction of total OA that is internally mixed with BC decreases as [OA]/[rBC] increases. We

486   assume that the population of particles containing BC exhibit faster loss than the population that

487   does not. Independent of the enhanced decay for BC-rich particles, particle decay is faster than for

488   dilution-driven decay of gases because the particles are more subject to wall losses. The reference

489   decay rates for particles and gases were determined from experiments conducted using atomized

490   ammonium sulfate, atomized fullerene soot, and a "dark" smoke experiment. It is assumed that

Atmospheric
Chemistry
and Physics
Discussions

491   POA does not evaporate upon dilution in the chamber, and thus does not contribute further to the

492   available NMOG, discussed further in Section 3.2.6.

493   **SOA properties and model fitting:** The different types of SOA in the model, which form

494   from different NMOG, can have different properties. The properties that are allowed to differ

495   between SOA types and heterogeneous oxidation products, besides k_{OH}, are the MAC_{BrC}, SOA

496   yields, O:C, and the f_{60} (**Table 1** and **Table 2**). While allowed to vary between SOA type, these

497   parameters are assumed to be independent of the SSA class. In this manner, we aim to find an

498   overall solution that allows for one set of SOA-type specific parameters that gives good model-

499   measurement agreement for all of the SSA classes. The choice of SOA yields influences all model

500   outputs, while the choice of the other parameters influence only that parameter output. The type-

501   specific MAC_{BrC} and SOA yields (α) are determined by fitting the model to the observations,

502   specifically to the evolution of [OA]/[rBC] and MAC_{BrC} with the OH exposure (**Table 1**). The

503   Global Fit package in Igor v.8.03 (Wavemetrics) allowed for simultaneous fitting of the observed

504   [OA]/[rBC] and MAC_{BrC} for all particle classes. Thus, the retrieved MAC_{BrC} and α values are those

505   that minimize the model-observation difference across all of the particle classes. After determining

506   the best-fit, type-specific MAC_{BrC} and SOA yields, separate global fits were performed to the

507   observed O:C and f_{60} to determine the type-specific O:C and f_{60} (**Table 1**).

508   Our analysis focuses on the evolution of the particle optical properties, and specifically the

509   BrC absorptivity. Section 3.2.2 provides a detailed discussion of the evolution of the MAC_{BrC} with

510   oxidation and the associated determination of SOA-type specific MAC_{BrC} values. Values for the

511   other parameters (SOA yields, O:C and the f_{60}) are briefly discussed here. The tuned SOA yields

512   were $\alpha_{fast} = 0.43$, $\alpha_{slow} = 0.15$, $\alpha_{VS} = 0.05$, and $\alpha_{MG} = 0.45$. These are effective yields averaged

513   across all NMOG of a given type. The derived average SOA yields are within the range of SOA

514   yields expected for the individual precursor species (Bruns et al., 2016).

515   Tuned values for the O:C for the SOA types are consistent with expected physical behavior,

516   guided by single-component studies (Chhabra et al., 2011). The fit O:C atomic ratios of the first-

517   generation SOA formed are 0.73 (fast), 0.59 (slow), and 0.59 (very slow, assumed the same as

518   slow). The O:C of multi-generation SOA and heterogeneously oxidized POA and SOA vary with

519   time, with the model fit indicating 1.22 oxygen atoms added per oxidation reaction, generally

520   consistent with expectations (Kroll et al., 2015). The observed AMS f_{60} rapidly falls to 0.008. To

18

521   match the observed behavior the fit $f_{60,fast} = 0.008$, $f_{60,slow} = f_{60,VS} = 0.003$, $f_{60,MG} = 0.006$, and the

522   f_{60} for products of heterogeneous oxidation dependent on whether SOA ($f_{60,het} = 0.01$), externally

523   mixed POA ($f_{60,het} = 0.003$), or internally mixed POA ($f_{60,het} = 0.008$) reacts. We note that similar

524   results are obtained if $f_{C2H4O2+}$ values are used instead of f_{60}. ($f_{C2H4O2+}$ is the high-resolution ion at

525     $m/z = 60$ that most corresponds to levoglucosan.)

3.2.2 Model-measurement comparison

527   The optimized model does a good job (reduced chi-square = 0.4) of describing the evolution

528   of MAC_{BrC}, [OA]/[rBC], O:C atomic ratio, and AMS f_{60} (**Figure 3**). The reasonable agreement for

529   [OA]/[rBC] indicates the appropriateness of the empirical correction for enhanced decay of rBC-

530   containing particles, the specified SOA yields and initial [NMOG]/[OA] ratio, and the

531   apportionment between the different NMOG types. The model-measurement agreement improves

532   if the unknown model parameters are allowed to vary somewhat between particle classes; again,

533   some variability is expected given the burn-to-burn variability in the mix of NMOG species

534   (Sekimoto et al., 2018). However, that use of class-independent parameters provides for a

535   generally good description across classes demonstrates an overall general nature of the

536   photochemical evolution.

537   The evolution of the MAC_{BrC}, [OA]/[rBC], O:C atomic ratio, and AMS f_{60} derive from changes

538   in the OA composition. Examples of the simulated time-dependent variation in OA composition

539   for particle class 1 and class 6 are shown in **Figure 4**. The observations demonstrate the importance

540   of SOA formation, with the predicted fractional contribution of POA decreasing over time. For

541   class 1, the MAC_{BrC} decays rapidly owing to a large fraction of the POA being internally mixed

542   with BC and therefore subject to enhanced decay in our experiments. Importantly, simulations

543   with heterogeneous oxidation only (i.e., no SOA formation is allowed) show much too small

544   increases in [OA]/[rBC] values and too slow decay of the AMS f_{60} and rise of the O:C (**Figure**

545   **S17**), discussed further in Section 3.2.4.

546   SOA type-specific MAC_{BrC} values determined from the model were $MAC_{fast} = 0.81$ (± 0.2) m^2

547   g^{-1}, $MAC_{slow} = MAC_{VS} = 0.05$ ($^{+0.05}_{-0.025}$) m^2 g^{-1}, $MAC_{2G} = 0.17$ (± 0.05) m^2 g^{-1}, and $MAC_{het} = 0.05$ (±

548   0.025) m^2 g^{-1}. The SOA$_{fast}$ is substantially more absorbing than the other SOA types. It is difficult

549   to estimate a comprehensive uncertainty on these values; the above uncertainties were qualitatively

550   estimated based on the model sensitivity to changing the parameter values (see Supplementary

Atmospheric
Chemistry
and Physics
Discussions
Open Access
EGU

551   Material). The strong absorptivity of the fast-forming SOA and the substantial difference between

552   MAC_{fast} and MAC_{slow} and MAC_{2G} are unexpected and somewhat surprising. The identities of the

553   likely precursor NMOG characterized (Koss et al., 2018) can be interrogated to understand this

554   difference along with the evolving chemical conditions in the chamber.

555   The measurements indicate precursor NMOG most likely to contribute to fast SOA formation

556   include: monoterpenes, guaiacol, benzenediol, methyl furfural, methyl guaiacol, vanillin, vinyl

557   guaiacol, creosol, isoeugenol, syringol, and styrene (**Figure S12**). The precursor NMOG most

558   likely to contribute to slow SOA formation include: toluene, 2-furanmethanol, phenol, o-cresol,

559   highly oxygenated levoglucosan dehydration products, naphthalene, tolualdehyde, 5-

560   hydroxymethyl tetrahydro 2-furanone, and C9 aromatic species. Benzene is the most likely very

561   slow SOA contributor, although contributes little here. These species are identified based on their

562   (i) measured emission factors and (ii) reaction rates with OH radicals (Koss et al., 2018), and (iii)

563   their estimated SOA yields (Bruns et al., 2016).

564   SOA absorptivity varies between precursors (Lambe et al., 2013;Romonosky et al., 2016;Xie

565   et al., 2017), suggesting different precursors contribute differentially to the SOA absorption here.

566   Monoterpenes form SOA that is non-to-weakly absorbing. In contrast, SOA from aromatic

567   precursors can be quite absorbing, more so in the presence of NO_x. Formation of nitro-aromatics

568   is often linked to the enhanced absorptivity when NO_x is present, and condensed phase reactions

569   producing highly conjugated, potentially N-containing compounds also contribute to light

570   absorption (Laskin et al., 2015). Garmash et al. (2020) recently reported ROOR' dimer formation

571   in the gas phase from OH oxidation of aromatics, which we speculate could also contribute to light

572   absorption.

573   Given the potential importance of nitro-aromatic formation to SOA light absorption, the

574   organonitrogen (ON) aerosol contribution here is characterized from the HR-AMS using the

575   method of Kiendler-Scharr et al. (2016) (see Supplemental Material in McClure et al. (2019)). (We

576   use the term "organonitrogen" quite generally here, as the measurements do not directly provide

577   the particular chemical nature of the N-containing organic species, which could be nitro-aromatics

578   or organic nitrates. Further work is required to quantitatively differentiate ON functionalities in

579   the AMS.) The [ON]/[OA] ratio for primary particles varies by SSA class and inversely with

580   [OA]/[rBC], from 5.7% (class 1) to 0.25% (class 6) (McClure et al., 2019). Upon oxidation, the

Atmospheric
Chemistry
and Physics
Discussions

Open Access

EGU

581 [ON]/[OA] ratio exhibits an initial rapid increase for all SSA classes (**Figure 5** and **Figure S18**),

582 demonstrating rapid formation of ON linked to oxidation of the fast-reacting NMOG. However,

583 over time the [ON]/[OA] ratio decreases for all SSA classes, with the exception of class 6 which

584 remains approximately constant. The slow and very slow NMOG and the MG species are,

585 apparently, comparably less likely to form ON in our experiments, leading to a decline in their

586 relative contribution to OA.

587 That the observed [ON]/[OA] ratio first increases then decreases with aging while the average

588 MAC_{BrC} derived for the SOA decreases with aging (owing to the $MAC_{fast} > MAC_{2G} > MAC_{slow} =$

589 MAC_{VS}) suggests a relationship between the processes driving these behaviors as well as a shift

590 with aging. While the [ON]/[OA] ratio would depend on the formation of any organonitrogen

591 species, the SOA absorption likely depends, at least in part, on nitro-aromatic formation. Organic

592 nitrates form from reaction of NO with peroxy radicals (RO_2), which competes with $RO_2 + HO_2$,

593 $RO_2 + RO_2$, and RO_2 autoxidation and is thus sensitive to variations in the availability of NO

594 (Orlando and Tyndall, 2012;Bianchi et al., 2019). However, nitro-aromatics typically form in the

595 gas phase from reaction of NO_2 with phenoxy radicals or with OH/aromatic adducts (Grosjean,

596 1984;Berndt and Böge, 2003;Vereecken, 2019). Phenoxy radicals generally derive from OH

597 reaction with phenolic molecules and both NO and O_3 compete with NO_2 for reaction with

598 phenoxy radicals; products from reaction with NO and O_3 are not well established (Vereecken,

599 2019). The importance of the OH-aromatic adduct + NO_2 pathway to nitro-aromatic formation is

600 suggested as small for species such as toluene and phenol owing to efficient reaction with O_2

601 (Atkinson et al., 1992;Vereecken, 2019), although has been proposed as the major pathway for

602 nitro-aromatic formation from guaiacol and similar species (Lauraguais et al., 2014;Sun et al.,

603 2019).

604 The [NO]/[NO₂] ratio in the primary smoke varied from 4.88 to 0.84 (Selimovic et al., 2018).

605 Modeling by Coggon et al. (2019) for a few of the experiments indicates a rapid decrease in the

606 [NO]/[NO₂] ratio towards zero with time owing to inefficient photolysis of NO_2 in the mini

607 chamber. Consequently, organic nitrate formation should be fastest early on, becoming very small

608 as time progresses. This can help explain the observed dependence of [ON]/[OA] on aging.

609 However, as nitro-aromatic formation involves NO_2, rather than NO, the evolving [NO]/[NO₂]

610 would not explain the evolution of the MAC_{BrC}. The fast reacting aromatics (e.g., guaiacol,

611 syringol, eugenol, styrene, vanillin, vinyl guaiacol, creosol, catechol) tend to be more substituted

Atmospheric
Chemistry
and Physics
Discussions

Open Access

EGU

612 than the slow reacting (e.g., phenol, o-cresol, toluene, benzaldehyde, tolualdehyde, naphthalene).

613 SOA formed from guiaiacol with NO_x present is substantially more absorbing than SOA from

614 either toluene or m-xylene (Romonosky et al., 2016). Additionally, the nitro-aromatic yield from

615 reaction of guaiacol exceeds that of phenol, reflecting, in part, faster H-abstraction from the phenol

616 group in more substituted aromatics (Harrison et al., 2005;Lauraguais et al., 2014), and production

617 of nitro-aromatic species from reaction of non-phenolic molecules, such as toluene, requires

618 multiple reactions with OH. Thus, it may be that the fast reacting aromatic species generally

619 produce more absorbing nitro-aromatic species and with higher SOA yields compared to the slow

620 reacting aromatic species, contributing to the decrease in both the [ON]/[OA] and the MAC_{BrC} with

621 aging in the mini chamber.

622 Analogous to the treatment of the MAC_{BrC} for SOA, we have attempted to model the ON

623 formation by assigning a NMOG type-specific, yet particle class-independent ON yield. Unlike

624 the MAC_{BrC}, no model parameters allow for good model-measurement agreement using this

625 approach. This primarily results from the different particle classes having very different

626 [ON]/[OA]. For example, for the [ON]/[OA] ratio for class 1 particles to increase from the initial

627 value (5.7%) to the peak value (18%) requires a much larger model ON species SOA yield than

628 for the class 6 particles, for which the [ON]/[OA] increases from 0.3% to only 0.6%. The reason

629 for these substantial differences likely relates to the factors discussed above.

630 The reasonableness of the derived MAC_{BrC} values for SOA is assessed by estimating

631 approximate upper (high-NO_x) and lower (low-NO_x) MAC_{BrC} values for the SOA types based on

632 literature MAC values for SOA from individual precursors (Romonosky et al., 2016), the NMOG

633 emission factors (Koss et al., 2018), and estimated SOA yields (Bruns et al., 2016):

634 $$MAC_{BrC,x} = \frac{\sum_i EF_i \cdot \alpha_i \cdot MAC_{BrC,i}}{\sum_i EF_i \cdot \alpha_i} \qquad (7.)$$

635 where x is the SOA type and i is for an individual NMOG. We note the highly uncertain nature of

636 these estimates and therefore only consider them qualitatively. The estimated $MAC_{BrC,fast}$ fall in

637 the range 0.3 m^2 g^{-1} (low-NO_x) to 2.4 m^2 g^{-1} (high-NO_x). This encompasses contributions from

638 highly absorbing and abundant guaiacol SOA, moderately absorbing benzene diol (and related

639 species), and effectively non-absorbing monoterpene SOA. For slow SOA, the estimated

640 $MAC_{BrC,slow}$ ranges from 0.1 m^2 g^{-1} to 0.6 m^2 g^{-1}, encompassing major contributions from

641 moderately absorbing phenol and cresol SOA. The estimated $MAC_{BrC,vs}$ depends almost entirely

642   on the benzene SOA, ranging from 0.21 m^2 g^{-1} (low-NO_x) to 0.88 m^2 g^{-1} (high-NO_x). Our derived

643    $MAC_{BrC,fast}$ falls between the upper and lower estimates, while the $MAC_{BrC,slow}$, $MAC_{BrC,VS}$, and

644    $MAC_{BrC,MG}$ are more similar to the lower estimates.

645   3.2.3 Extending the mini chamber results to the atmosphere

646   In the experiments, particles and gases experience different decay rates, with particle loss rates

647   exceeding NMOG precursor loss rates and the loss rates of BC-rich particles enhanced. The model

648   allows for simulation of the evolution of the overall system in the absence of such experimental

649   differences by setting the dilution of all components to the same value and wall losses to zero. This

650   provides insights into the likely influence of photochemical oxidation on the evolution of smoke

651   in the atmosphere, although likely does not fully account for the influence of NO_x and the evolving

652   NO/NO_2 ratio. For simplicity, we use a dilution rate of zero for these "atmospheric" simulations,

653   but any value could be used so long as the focus is on variability in intensive properties.

654   Simulated OA composition profiles are compared for particle classes 1 and 6, as examples, for

655   chamber ("chm") and atmospheric ("atm") simulations in **Figure 4**. In the atmospheric

656   simulations, the POA influence persists to much longer times than in the chamber simulations. For

657   example, for class 1 the POA fraction after 2 days of equivalent aging is 0.05 for the chamber

658   simulation but 0.35 for the atmospheric simulations; for class 6 the increase in the POA fraction,

659   from 0.2 (chamber) to 0.3 (atmospheric), is smaller, but still notable. Some of the increase in the

660   POA contribution for the atmospheric versus chamber simulations results from the POA and

661   NMOG having the same loss rates in the atmospheric simulations. This leads to a decreased

662   relative contribution of SOA. The larger difference between the atmospheric and chamber

663   simulations for particle class 1 also reflects the comparably greater influence of enhanced decay

664   of BC-rich particles.

665   The fractional contribution of the 2nd generation SOA decreases in the atmospheric

666   simulations, for all classes. This too results from the particle decay rate equaling the gas decay rate

667   in the atmospheric simulations. In the chamber simulations, the OA is lost at a faster rate than the

668   gases, and thus the 2nd generation SOA, which forms later than the fast and slow SOA, is

669   effectively enhanced; this enhancement does not influence the atmospheric simulations. There is

670   little difference in the fractional contribution of heterogeneous oxidation products between

671   simulations, a consequence of the ensemble treatment of heterogeneous oxidation products here.

Atmospheric
Chemistry
and Physics
Discussions

672   Differences between the chamber and atmospheric simulations are shown in **Figure 6** for the

673     $MAC_{BrC,405}$, [OA]/[rBC], O:C, AMS f_{60}, and the [SOA]/[POA] ratio. Averages across all particle

674   classes are shown to facilitate comparison; atmospheric simulation results for individual particle

675   classes are compared with the observations in **Figure S19**. Given the relatively large (albeit

676   particle class-dependent) absorptivity of the POA, the $MAC_{BrC,atm}$ decays more slowly than the

677     $MAC_{BrC,chm}$. This is accentuated by the fraction of fast SOA being somewhat greater at longer aging

678   times for the atmospheric simulations, since the $MAC_{fast} > MAC_{sec} > MAC_{slow}$. The evolution of the

679   MAC_{BrC} for the atmospheric simulations is empirically well described by a bi-exponential decay.

680   A fit to the model prediction for the average behavior across all classes (**Figure 6**) yields time

681   constants of 0.4 day and 2.8 days. (The overall fit equation is: $MAC_{BrC} = 0.29 + 0.59 \cdot \exp(-t_{OH}/2.8)$

682     $+ 0.13 \cdot \exp(-t/2.78)$, where t_{OH} is in days and the MAC_{BrC} in m^2 g^{-1}.)

683   Additionally, the increase in the [OA]/[rBC] is much smaller in the atmospheric simulations

684   and the O:C values somewhat smaller. The AMS f_{60} at longer aging times remain similar to the

685   observations but are somewhat larger at shorter times for the atmospheric simulations. The

686   ([SOA]+[POA$_{ox}$])/[POA] is substantially smaller for the atmospheric simulations, with the

687   difference growing over time. After $t_{OH} = 1$ day the geometric average atmospheric

688   ([SOA]+[POA$_{het}$])/[POA] equals 1.7 while the chamber ([SOA]+[POA$_{het}$])/[POA] equals 3.7.

689   After $t_{OH} = 6$ days the atmospheric ([SOA]+[POA$_{het}$])/[POA] equals 5.8 while the chamber

690   ([SOA]+[POA$_{het}$])/[POA] equals 20.8.

691 ### 3.2.4 Secondary OA versus heterogeneous oxidation

692   The particle properties evolve from both SOA formation and heterogeneous oxidation. To

693   separate these processes, two additional sets of model simulations are run: (i) with the gas-phase

694   rate coefficients set to zero such that only heterogeneous oxidation occurs, and (ii) with the OH

695   uptake coefficient set to zero, and thus only SOA formation occurs (**Figure 6**). It is evident that

696   the evolution of all intensive properties occurs much more slowly with only heterogeneous

697   oxidation. With heterogeneous oxidation only, the class-average $MAC_{BrC,405}$ decays to a much

698   lesser extent, even for the atmospheric simulations. Similarly, the increase in O:C is much too

699   small and the AMS f_{60} decays to a much lesser extent. The OA-to-BC ratio for the heterogeneous-

700   only simulations differ notably from the full simulations. For the heterogeneous-only chamber

701   simulations, this ratio increases initially until about 1.5 days of aging, at which point it decreases.

702 The decrease results from loss of mass over time from fragmentation, while the increase results

703 from faster loss of BC-rich particles in the chamber. For the atmospheric simulations, the OA-to-

704 BC ratio decreases continuously when only heterogeneous oxidation is included. In contrast, for

705 most properties the SOA-only simulations differ by only small amounts from the full simulations.

706 The exception is the MAC_{BrC}, for which the decrease in the class-average value with time is notably

707 smaller in the SOA-only simulation compared to the full simulation for both chamber and

708 atmospheric simulations. Our simulations assumed an OH reactive uptake coefficient of unity. We

709 note that if a substantially larger value is assumed ($\gamma_{OH} \sim 10$), the predicted changes due to

710 heterogeneous oxidation are much larger and reasonably in line with the observations. Values

711 substantially greater than unity have been found for some chemical systems (Richards-Henderson

712 et al., 2016;Schnitzler and Abbatt, 2018), but for compounds such as levoglucosan—a notable

713 component of BB particles—values less than unity are common (Kroll et al., 2015).

714 Under the assumption that $\gamma_{OH} \leq 1$ for BB particles, these observations point to an important

715 conclusion that is in line with various ambient observations. Large changes in key intensive

716 properties of BB particles, such as O:C, and AMS f_{60}, result primarily from secondary OA

717 formation, with heterogeneous oxidation having a smaller influence. While the BrC absorptivity

718 is comparably more sensitive to heterogeneous oxidation, SOA formation remains the major driver

719 of the observed changes. Thus, in ambient observations of biomass burning plumes (Vakkari et

720 al., 2014;Forrister et al., 2015;Garofalo et al., 2019), a notable increase in the O:C (or related

721 measures) and a decrease in the f_{60} can be taken as a clear indication of SOA formation.

722 ### 3.2.5 Absolute absorption

723 The observations indicate that the observable (i.e. bulk average) MAC_{BrC} decreases with

724 photochemical aging. However, this results primarily from mixing of absorbing POA with various

725 types of absorbing SOA, with some contribution from heterogeneous oxidation. As such, the

726 absolute absorption in the atmospheric simulations typically increases over time, at least initially,

727 due to the production of new, absorbing particle mass. The exact behavior is particle class-specific

728 (**Figure 7**). The initial increase slows over time as the pool of NMOG precursors depletes. At even

729 longer times the absolute absorption for some classes decreases as heterogeneous oxidation

730 converts more absorbing BrC (specifically, POA and SOA_{fast}) into less absorbing BrC and

731 engenders some mass loss over time due to fragmentation. However, this is only true for some of

732   the particle classes. The simulations indicate that, on average, after one day of equivalent aging

733   the absolute absorption increases by a factor of 1.6 owing to production of new, absorbing OA

734   mass.

735

3.2.6 POA volatility and the impact of dilution

737   Upon dilution, semi-volatile particle components may evaporate, which should lead to a

738   decrease in the OA-to-BC ratio and, potentially, changes in other particle properties; the MAC_{BrC}

739   could change if the absorptivity of the evaporating versus low-volatility (or non-volatile)

740   components differ. Given the semi-batch operation (Section 2.2) substantial, continual dilution

741   occurs throughout an experiment. Rapid dilution also occurs upon sampling of smoke into the

742   clean mini chamber air. Dilution-driven evaporation has been suggested as an important factor in

743   the chemical evolution of BB in ambient biomass burning plumes (Hodshire et al., 2019).

744   We assessed the impact of continual dilution on our observations by conducting one

745   experiment during which the chamber was left dark, although ozone was present at about 50 ppb

746   (**Figure 8**). The primary particles corresponded to class 3 particles (SSA_{405nm} = 0.73). After

747   sampling, the OA and rBC concentrations decreased by about a factor of 33 over 45 minutes owing

748   to dilution and other losses. For comparison, the [ACN] dilution tracer decreased by a factor of 21.

749   During this experiment the [OA]/[rBC] ratio was nearly constant (19.6 ± 0.7, 1σ), even slightly

750   increasing over time. Also, the O:C remained constant (0.39 ± 0.03, 1σ), as did the H:C ($1.74 \pm$

751   0.01, 1σ). These observations together indicate that there was little, if any, evaporative loss of OA.

752   However, the AMS f_{60} declined continually, by about 30%. The signal at $m/z = 60$ is only a small

753   fraction of the total OA, and thus changes in f_{60} can occur even if only small changes in total mass

754   occur. The AMS f_{60} could also evolve over time from in-particle reactions that occur even in the

755   absence of oxidants. The mass fraction of OA remaining (MFR_{OA}) after heating in the

756   thermodenuder increased slightly over time, from 0.05 to 0.07. This could indicate evaporation of

757   more volatile components, although could result from "ripening" of the particles over time

758   (Tritscher et al., 2011).

759   SOA from reaction of some NMOG with O_3 may have offset some evaporative OA mass loss,

760   keeping the total OA mass constant while the f_{60} and MFR_{org} changed. Monoterpenes are the most

761   important SOA precursor class here that reacts readily with O_3. The measured initial monoterpene

762   concentration (8.6 ppb = 50 µg m^{-3}) constrains the potential SOA formed. Accounting for

763   differential losses of particles and gases in the mini chamber, with 50 ppb O_3 and an assumed SOA

764   yield of 0.3, we estimate that SOA formation might have increased the [OA]/[rBC] ratio by about

765   4%. Given the constancy of the [OA]/[rBC], we estimate no more than 8% of the OA evaporated

766   despite the substantial dilution over the 45-minute experiment. Much greater POA evaporation is

767   expected based on the volatility distribution of May et al. (2013) for biomass burning OA,

768   assuming evaporation is facile. Using their distribution, we estimate a factor of 33 decrease in the

769   OA should have resulted in a decrease in the [OA]/[rBC] from 19.6 to 11.2 from evaporation; a

770   factor of 21 dilution (the observed value for ACN) should have caused a decrease to [OA]/[rBC]

771   = 10.5. Thus, we conclude that evaporation due to dilution had minimal influence on our

772   observations and, more broadly, suggests minimal influence of dilution in general.

773   The reason for the insensitivity to dilution of our experiments may result from the

774   concentration range considered. May et al. (2013) established the volatility distribution for

775   biomass burning OA from thermodenuder measurements. They compared predictions from their

776   derived volatility distribution to observations of OA emission factors for different fuel types at

777   varying levels of dilution and initial concentrations. At the lowest initial [OA] (~100 µg m^{-3}),

778   active dilution had little influence and in some cases the OA emission factor actually increased

779   after dilution in their experiments. In contrast, when the initial [OA] was much larger, on order of

780   1000 µg m^{-3}, there was a clearer relationship between the OA emission factor and the OA

781   concentration and better agreement with their predictions. For comparison, in our experiments, the

782   initial [OA] in the mini chamber had a geometric average of 76 µg m^{-3}, ranging from 8 µg m^{-3} to

783   384 µg m^{-3}; notably, the dark experiment was at the highest initial [OA]. Dilution into the mini

784   chamber was a factor of seven. Most likely, evaporation resulting from dilution occurred upon

785   initial injection of the particles into the mini chamber with little additional evaporation as

786   experiments progressed, to the extent that the particles evaporated much at all.

787   **3.3   Comparison with ambient observations**

788   There are very few ambient assessments of how photochemical oxidation influences brown

789   carbon absorptivity. Forrister et al. (2015) measured dilution-corrected water-soluble + methanol-

27

790   soluble BrC absorption in ambient wildfire plumes at various distances downwind from the fires.

791   The measured O:C and AMS f_{60} changed with time as the BrC absorption decreased, indicating

792   that chemical changes occurred as the plume aged. They observed that the absolute BrC absorption

793   decreased over time, with a timescale of only 10 h. This decay time for BrC is substantially faster

794   than we observe for any of the particle classes. Interestingly, we predict that over 10 h the

795   absorption by BrC in a wildfire plume should have increased, and only at much later times should

796   have decreased (**Figure 7**). In the case where only heterogeneous oxidation is included (with γ_{OH}

797   = 1), the predicted decay in BrC absorption based on our observations has a timescale of ca. 4

798   days, substantially slower than observed by Forrister et al. (2015).

799   It is possible that the smoke sampled by Forrister et al. (2015) differed significantly from any

800   of the burns sampled here. However, this seems unlikely given the wide-range of fuels and burn

801   conditions considered here, and since the plumes sampled by Forrister et al. (2015) likely derived

802   from combustion of similar fuels as used here. Also unlikely is that greater dilution in the

803   atmosphere played an important role, as it is thought that more absorbing primary OA has lower

804   volatility than less absorbing primary OA (Saleh et al., 2014). Thus, it is possible that the difference

805   between Forrister et al. (2015) and our results indicates that direct photobleaching rapidly degrades

806   BrC absorptivity, as direct photolysis in our experiments was likely of minimal importance owing

807   to the relatively low light intensity, single initiation wavelength (254 nm), and short absolute

808   timescale (<1 h) compared to the atmosphere.

809   However, an additional difference is that we measured absorption by suspended particles at

810   low-to-moderate relative humidity whereas Forrister et al. (2015) characterized BrC absorption

811   after extracting material collected onto filters into water and then methanol. It is possible that

812   solvent extraction alters the BrC absorptivity in some OA-composition-dependent manner, leading

813   to an apparent time-dependent decay in the BrC absorption. Consistent with this suggestion,

814   Fleming et al. (2020) reported that (i) the total absorptivity lifetime of BB particles photolytically

815   aged on a filter greatly exceeded those of individual chromophores (>10 days versus <2 days), and

816   (ii) the apparent changes in total absorption depended on whether the absorption was measured for

817   particles on the filter versus for solution extracts. Nonetheless, this suggestion remains speculative

818   as direct, quantitative comparisons between BrC absorption measured for suspended particles

819   versus from solution extracts are limited; we suggest that targeted comparisons between absorption

820   measurement methods would be informative.

821   Wang et al. (2016) also characterized changes in BrC absorptivity of BB particles in the

822   Amazon. They found that the BrC absorptivity decreased initially over an estimated ca. 20 h of

823   photochemical aging, after which the absorptivity remained constant. As above, this timescale

824   seems too short for heterogeneous oxidation to have a major impact, thus implicating direct

825   photolysis as the reason for the photobleaching. However, there are two important considerations.

826   First, Wang et al. (2016) note that they cannot rule out production of less absorbing SOA as the

827   reason for the absorptivity decrease. While the OA concentration was constant over time and

828   therefore suggestive of little SOA formation, it may be that dilution of the plume offset SOA

829   formation and consequently that SOA formation precipitated the decrease in absorptivity. Second,

830   their estimated lifetimes are determined from NO_x losses, and thus sensitive to assumptions about

831   the average OH; as such, longer lifetimes cannot be ruled out.

832   Finally, Zhang et al. (2017) characterized water + methanol extracted BrC in the outflow of

833   storm clouds and, in one case, were able to measure BrC absorption for freshly expelled versus

834   particles sampled one day later. The BrC absorption for the fresh and aged particles were nearly

835   identical, with no indication of bleaching despite the high altitude, 11 km, and thus high UV photon

836   flux. Thus, this study indicates that photobleaching of BrC may have little influence on at least

837   some types of BrC. Further, Zhang et al. (2017) report absolute absorption values that, it seems,

838   are not dilution corrected. Thus, the constancy of the absolute absorption between the fresh and

839   aged particles implies potential BrC production, as dilution is expected. Ultimately, further

840   experiments investigating direct photolysis of biomass-derived BrC and additional field

841   observations of the evolution of BrC absorptivity will be necessary to reconcile our findings and

842   the limited number of field observations.

843

844   **4   Conclusions**

845   We characterized the photochemical evolution of smoke (particles + gases) produced from

846   combustion of a wide variety of biomass fuels. Particle properties were characterized as a function

847   of equivalent photochemical aging, with a focus on the particle optical properties. Photochemical

848   aging led to dramatic changes in the particle chemical composition, as evidenced by a large and

29

849 rapid increase in the O:C atomic ratio of the organic aerosol and a decrease in the marker ion f_{60}

850 in the OA mass spectrum. These chemical changes occurred concurrent with large changes in the

851 [OA]/[rBC] ratio, indicating substantial production of secondary organic aerosol mass. The

852 particle optical properties also changed substantially upon aging. Experiments were classified into

853 six classes according to the SSA of the primary particles. The average evolution of the optical

854 properties of particles in each class was characterized; the observed behavior was generally class-

855 specific. The total particle absorptivity normalized to black carbon (the MAC_{BC}) generally

856 increased with aging due to production of new, somewhat absorbing OA. The single scatter albedo

857 also generally increased with aging, although to a much less extent for experiments in which the

858 initial particles already had a large SSA. The absorptivity of the organic aerosol components, i.e.

859 of the brown carbon mass absorption coefficient (MAC_{BrC}), exhibited class-specific behavior. For

860 particles having an initially large SSA, the MAC_{BrC} exhibited an initial increase at short times (<0.5

861 days of equivalent aging) but then decreased monotonically with continued aging. For particles

862 having an initially small SSA, there was a rapid decline in the MAC_{BrC} at short times and then a

863 continued slower decline at longer times. At long times the MAC_{BrC} for the high SSA and low SSA

864 initial particles behaved similarly.

865 The evolution of the BrC absorptivity was shown to be consistent with a combination of

866 production of strongly absorbing and much more weakly absorbing secondary OA, along with

867 heterogeneous conversion of absorbing POA and SOA into a less absorbing oxidized OA. This

868 was the case for all particle classes. The SOA formed could be distinguished into four general

869 types: (i) a fast-forming, relatively highly absorbing type; (ii) a more slowly-forming, weakly

870 absorbing type; (iii) a very slowly forming, weakly absorbing type; and (iv) a weakly absorbing,

871 second-generation type. The relative abundances of these different types were similar between the

872 different particle classes. The combination of SOA formation and heterogeneous oxidation causes

873 the MAC_{BrC} to evolve in time on three timescales: (i) an initial rapid increase occurring at aging

874 times < 0.25 days, (ii) a moderately fast decrease, occurring with a timescale of ~ 1day, and (iii) a

875 longer decay, occurring with a time scale of about ~ 1 week. Our results demonstrate that, while

876 primary particle properties derived from biomass combustion can vary dramatically in terms of

877 their properties, the overall evolution upon photochemical aging is reasonably independent of the

878 initial conditions.

30

5   Data Availability

All data used to create this manuscript are available at: http://www.esrl.noaa.gov/csd/FIREX/.

6   Author Contributions

CDC and JHK designed the experiments. CDC, CYL, DHH, MC, AK, TBO and KS carried out the measurements and data processing, with additional assistance from CW and JdG. CDC and CL analyzed data. CDC wrote the manuscript, with contributions from all co-authors.

7   Acknowledgement

8   Financial support

9   References

Andreae, M. O., and Merlet, P.: Emission of trace gases and aerosols from biomass burning, Global Biogeochemical Cycles, 15, 955-966, https://doi.org/doi:10.1029/2000GB001382, 2001.

Andreae, M. O., and Gelencser, A.: Black carbon or brown carbon? The nature of light-absorbing carbonaceous aerosols, Atmospheric Chemistry and Physics, 6, 3131-3148, https://doi.org/10.5194/acp-6-3131-2006, 2006.

Atkinson, R., Aschmann, S. M., and Arey, J.: Reactions of OH and NO_3 radicals with phenol, cresols, and 2-nitrophenol at 296 +/- 2 K, Environmental Science & Technology, 26, 1397-1403, https://doi.org/10.1021/es00031a018, 1992.

Aumont, B., Szopa, S., and Madronich, S.: Modelling the evolution of organic carbon during its gas-phase tropospheric oxidation: development of an explicit model based on a self generating approach, Atmos. Chem. Phys., 5, 2497-2517, https://doi.org/10.5194/acp-5-2497-2005, 2005.

Berndt, T., and Böge, O.: Gas-phase reaction of OH radicals with phenol, Physical Chemistry Chemical Physics, 5, 342-350, https://doi.org/10.1039/B208187C, 2003.

910   Bianchi, F., Kurten, T., Riva, M., Mohr, C., Rissanen, M. P., Roldin, P., Berndt, T., Crounse, J.
911   D., Wennberg, P. O., Mentel, T. F., Wildt, J., Junninen, H., Jokinen, T., Kulmala, M., Worsnop,
912   D. R., Thornton, J. A., Donahue, N., Kjaergaard, H. G., and Ehn, M.: Highly Oxygenated
913   Organic Molecules (HOM) from Gas-Phase Autoxidation Involving Peroxy Radicals: A Key
914   Contributor to Atmospheric Aerosol, Chemical Reviews, 119, 3472-3509,
915   https://doi.org/10.1021/acs.chemrev.8b00395, 2019.

916   Bond, T. C., Streets, D. G., Yarber, K. F., Nelson, S. M., Woo, J.-H., and Klimont, Z.: A
917   technology-based global inventory of black and organic carbon emissions from combustion, J.
918   Geophys. Res., 109, D14203, https://doi.org/10.1029/2003jd003697, 2004.

919   Browne, E. C., Zhang, X., Franklin, J. P., Ridley, K. J., Kirchstetter, T. W., Wilson, K. R.,
920   Cappa, C. D., and Kroll, J. H.: Effect of heterogeneous oxidative aging on light absorption by
921   biomass burning organic aerosol, Aerosol Science and Technology, 53, 663-674,
922   https://doi.org/10.1080/02786826.2019.1599321, 2019.

923   Bruns, E. A., El Haddad, I., Slowik, J. G., Kilic, D., Klein, F., Baltensperger, U., and Prévôt, A.
924   S. H.: Identification of significant precursor gases of secondary organic aerosols from residential
925   wood combustion, Scientific Reports, 6, 27881, https://doi.org/10.1038/srep27881, 2016.

926   Burtscher, H.: Measurement and characteristics of combustion aerosols with special
927   consideration of photoelectric charging and charging by flame ions, J Aerosol Sci, 23, 549-595,
928   https://doi.org/10.1016/0021-8502(92)90026-R, 1992.

929   Cappa, C. D., Onasch, T. B., Massoli, P., Worsnop, D., Bates, T. S., Cross, E., Davidovits, P.,
930   Hakala, J., Hayden, K., Jobson, B. T., Kolesar, K. R., Lack, D. A., Lerner, B., Li, S. M., Mellon,
931   D., Nuaanman, I., Olfert, J., Petaja, T., Quinn, P. K., Song, C., Subramanian, R., Williams, E. J.,
932   and Zaveri, R. A.: Radiative absorption enhancements due to the mixing state of atmospheric
933   black carbon, Science, 337, 1078-1081, https://doi.org/10.1126/science.1223447, 2012.

934   Cappa, C. D., and Wilson, K. R.: Multi-generation gas-phase oxidation, equilibrium partitioning,
935   and the formation and evolution of secondary organic aerosol, Atmos. Chem. Phys., 12, 9505-
936   9528, https://doi.org/10.5194/acp-12-9505-2012, 2012.

937   Cappa, C. D., Lim, C. Y., Hagan, D. H., and Kroll, J. H.: Measurements from the Fire Influence
938   on Regional and Global Environments Experiment (FIREX) Fire Lab Mini Chamber
939   Experiment, UC Davis DASH, Dataset, version 1, https://doi.org/10.25338/B8CK5N, 2019a.

940   Cappa, C. D., Zhang, X., Russell, L. M., Collier, S., Lee, A. K. Y., Chen, C.-L., Betha, R., Chen,
941   S., Liu, J., Price, D. J., Sanchez, K. J., McMeeking, G., Williams, L. R., Onasch, T. B., Worsnop,
942   D. R., Abbatt, J., and Zhang, Q.: Light absorption by ambient black and brown carbon and its
943   dependence on black carbon coating state for two California, USA cities in winter and summer,
944   Journal of Geophysical Research-Atmospheres, 124, 1,550-551,577,
945   https://doi.org/10.1029/2018JD029501, 2019b.

946   Cheng, Y., Engling, G., Moosmaller, H., Arnott, W. P., Chen, L. W. A., Wold, C. E., Hao, W.
947   M., and He, K. B.: Light absorption by biomass burning source emissions, Atmospheric
948   Environment, 127, 347-354, https://doi.org/10.1016/j.atmosenv.2015.12.045, 2016.

949   Chhabra, P. S., Ng, N. L., Canagaratna, M. R., Corrigan, A. L., Russell, L. M., Worsnop, D. R.,
950   Flagan, R. C., and Seinfeld, J. H.: Elemental composition and oxidation of chamber organic

951 aerosol, Atmospheric Chemistry and Physics, 11, 8827-8845, https://doi.org/10.5194/acp-11-
952 8827-2011, 2011.

953 Coggon, M. M., Lim, C. Y., Koss, A. R., Sekimoto, K., Yuan, B., Cappa, C. D., Kroll, J. H.,
954 Selimovic, V., Zarzana, K. J., Brown, S. S., Roberts, J. M., Müller, M., Yokelson, R. J.,
955 Wisthaler, A., Krechmer, J., Jimenez, J. L., De Gouw, J., and Warneke, C.: OH-chemistry of
956 volatile organic compounds emitted from laboratory and ambient biomass burning smoke:
957 Influence of furans and oxygenated aromatics on ozone and secondary VOC formation., Atmos.
958 Chem. Phys. Discuss., https://doi.org/10.5194/acp-2019-516, 2019.

959 Cross, E. S., Onasch, T. B., Ahern, A., Wrobel, W., Slowik, J. G., Olfert, J., Lack, D. A.,
960 Massoli, P., Cappa, C. D., Schwarz, J. P., Spackman, J. R., Fahey, D. W., Sedlacek, A.,
961 Trimborn, A., Jayne, J. T., Freedman, A., Williams, L. R., Ng, N. L., Mazzoleni, C., Dubey, M.,
962 Brem, B., Kok, G., Subramanian, R., Freitag, S., Clarke, A., Thornhill, D., Marr, L. C., Kolb, C.
963 E., Worsnop, D. R., and Davidovits, P.: Soot Particle Studies—Instrument Inter-Comparison—
964 Project Overview, Aerosol Science and Technology, 44, 592 - 611,
965 https://doi.org/10.1080/02786826.2010.482113, 2010.

966 Cubison, M. J., Ortega, A. M., Hayes, P. L., Farmer, D. K., Day, D., Lechner, M. J., Brune, W.
967 H., Apel, E., Diskin, G. S., Fisher, J. A., Fuelberg, H. E., Hecobian, A., Knapp, D. J., Mikoviny,
968 T., Riemer, D., Sachse, G. W., Sessions, W., Weber, R. J., Weinheimer, A. J., Wisthaler, A., and
969 Jimenez, J. L.: Effects of aging on organic aerosol from open biomass burning smoke in aircraft
970 and laboratory studies, Atmos. Chem. Phys., 11, 12049-12064, https://doi.org/10.5194/acp-11-
971 12049-2011, 2011.

972 Dale, V. H., Joyce, L. A., McNulty, S., Neilson, R. P., Ayres, M. P., Flannigan, M. D., Hanson,
973 P. J., Irland, L. C., Lugo, A. E., Peterson, C. J., Simberloff, D., Swanson, F. J., Stocks, B. J., and
974 Wotton, B. M.: Climate Change and Forest Disturbances: Climate change can affect forests by
975 altering the frequency, intensity, duration, and timing of fire, drought, introduced species, insect
976 and pathogen outbreaks, hurricanes, windstorms, ice storms, or landslides, BioScience, 51, 723-
977 734, https://doi.org/10.1641/0006-3568(2001)051[0723:CCAFD]2.0.CO;2, 2001.

978 Feng, Y., Ramanathan, V., and Kotamarthi, V. R.: Brown carbon: a significant atmospheric
979 absorber of solar radiation?, Atmos. Chem. Phys., 13, 8607-8621, https://doi.org/10.5194/acp-
980 13-8607-2013, 2013.

981 Fierce, L., Bond, T. C., Bauer, S. E., Mena, F., and Riemer, N.: Black carbon absorption at the
982 global scale is affected by particle-scale diversity in composition, Nat. Comm., 7,
983 https://doi.org/10.1038/ncomms12361, 2016.

984 Fierce, L., Onasch, T. B., Cappa, C. D., Mazzoleni, C., China, S., Bhandari, J., Davidovits, P.,
985 Fischer, D. A., Helgestad, T. M., Lambe, A., Sedlacek, A. J., Smith, G. D., and Wolff, L.:
986 Absorption enhancements by black carbon controlled by particle-to-particle heterogeneity in
987 composition, Proc. Nat. Acad. Sci., Accepted.

988 Fleming, L. T., Lin, P., Roberts, J. M., Selimovic, V., Yokelson, R., Laskin, J., Laskin, A., and
989 Nizkorodov, S. A.: Molecular composition and photochemical lifetimes of brown carbon
990 chromophores in biomass burning organic aerosol, Atmos. Chem. Phys., 20, 1105-1129,
991 https://doi.org/10.5194/acp-20-1105-2020, 2020.

992 Forrister, H., Liu, J., Scheuer, E., Dibb, J., Ziemba, L., Thornhill, K. L., Anderson, B., Diskin,
993 G., Perring, A. E., Schwarz, J. P., Campuzano-Jost, P., Day, D. A., Palm, B. B., Jimenez, J. L.,

994   Nenes, A., and Weber, R. J.: Evolution of brown carbon in wildfire plumes, Geophysical
995   Research Letters, 42, 4623-4630, https://doi.org/10.1002/2015GL063897, 2015.

996   Fortner, E., Onasch, T., Canagaratna, M., Williams, L. R., Lee, T., Jayne, J., and Worsnop, D.:
997   Examining the chemical composition of black carbon particles from biomass burning with SP-
998   AMS, J Aerosol Sci, 120, 12-21, https://doi.org/10.1016/j.jaerosci.2018.03.001, 2018.

999   Fuller, K. A., Malm, W. C., and Kreidenweis, S. M.: Effects of mixing on extinction by
1000   carbonaceous particles, J. Geophys. Res.-Atmos., 104, 15941-15954,
1001   https://doi.org/10.1029/1998jd100069, 1999.

1002   Garmash, O., Rissanen, M. P., Pullinen, I., Schmitt, S., Kausiala, O., Tillmann, R., Zhao, D.,
1003   Percival, C., Bannan, T. J., Priestley, M., Hallquist, Å. M., Kleist, E., Kiendler-Scharr, A.,
1004   Hallquist, M., Berndt, T., McFiggans, G., Wildt, J., Mentel, T. F., and Ehn, M.: Multi-generation
1005   OH oxidation as a source for highly oxygenated organic molecules from aromatics, Atmos.
1006   Chem. Phys., 20, 515-537, https://doi.org/10.5194/acp-20-515-2020, 2020.

1007   Garofalo, L. A., Pothier, M. A., Levin, E. J. T., Campos, T., Kreidenweis, S. M., and Farmer, D.
1008   K.: Emission and Evolution of Submicron Organic Aerosol in Smoke from Wildfires in the
1009   Western United States, ACS Earth and Space Chem., 3, 1237-1247,
1010   https://doi.org/10.1021/acsearthspacechem.9b00125, 2019.

1011   Grosjean, D.: Atmospheric reactions of ortho cresol: Gas phase and aerosol products,
1012   Atmospheric Environment, 18, 1641-1652, https://doi.org/10.1016/0004-6981(84)90386-X,
1013   1984.

1014   Harrison, M. A. J., Barra, S., Borghesi, D., Vione, D., Arsene, C., and Iulian Olariu, R.: Nitrated
1015   phenols in the atmosphere: a review, Atmospheric Environment, 39, 231-248,
1016   https://doi.org/10.1016/j.atmosenv.2004.09.044, 2005.

1017   Helgestad, T. M.: Characterizing the optical properties of coated black carbon particles, M.S.
1018   Thesis, Civil and Environmental Engineering, University of California, Davis, 2016.

1019   Hodshire, A. L., Akherati, A., Alvarado, M. J., Brown-Steiner, B., Jathar, S. H., Jimenez, J. L.,
1020   Kreidenweis, S. M., Lonsdale, C. R., Onasch, T. B., Ortega, A. M., and Pierce, J. R.: Aging
1021   Effects on Biomass Burning Aerosol Mass and Composition: A Critical Review of Field and
1022   Laboratory Studies, Environmental Science & Technology, 53, 10007-10022,
1023   https://doi.org/10.1021/acs.est.9b02588, 2019.

1024   Jacobson, M. Z.: Effects of biomass burning on climate, accounting for heat and moisture fluxes,
1025   black and brown carbon, and cloud absorption effects, Journal of Geophysical Research:
1026   Atmospheres, 119, 8980-9002, https://doi.org/10.1002/2014JD021861, 2014.

1027   Kiendler-Scharr, A., Mensah, A. A., Friese, E., Topping, D., Nemitz, E., Prevot, A. S. H., Äijälä,
1028   M., Allan, J., Canonaco, F., Canagaratna, M., Carbone, S., Crippa, M., Dall Osto, M., Day, D.
1029   A., De Carlo, P., Di Marco, C. F., Elbern, H., Eriksson, A., Freney, E., Hao, L., Herrmann, H.,
1030   Hildebrandt, L., Hillamo, R., Jimenez, J. L., Laaksonen, A., McFiggans, G., Mohr, C., O'Dowd,
1031   C., Otjes, R., Ovadnevaite, J., Pandis, S. N., Poulain, L., Schlag, P., Sellegri, K., Swietlicki, E.,
1032   Tiitta, P., Vermeulen, A., Wahner, A., Worsnop, D., and Wu, H.-C.: Ubiquity of organic nitrates
1033   from nighttime chemistry in the European submicron aerosol, Geophysical Research Letters, 43,
1034   7735-7744, https://doi.org/doi:10.1002/2016GL069239, 2016.

1035 Kirchstetter, T. W., Novakov, T., and Hobbs, P. V.: Evidence that the spectral dependence of
1036 light absorption by aerosols is affected by organic carbon, Journal of Geophysical Research-
1037 Atmospheres, 109, D21208, https://doi.org/10.1029/2004JD004999, 2004.

1038 Koss, A. R., Sekimoto, K., Gilman, J. B., Selimovic, V., Coggon, M. M., Zarzana, K. J., Yuan,
1039 B., Lerner, B. M., Brown, S. S., Jimenez, J. L., Krechmer, J., Roberts, J. M., Warneke, C.,
1040 Yokelson, R. J., and de Gouw, J.: Non-methane organic gas emissions from biomass burning:
1041 identification, quantification, and emission factors from PTR-ToF during the FIREX 2016
1042 laboratory experiment, Atmos. Chem. Phys., 18, 3299-3319, https://doi.org/10.5194/acp-18-
1043 3299-2018, 2018.

1044 Kroll, J. H., Lim, C. Y., Kessler, S. H., and Wilson, K. R.: Heterogeneous Oxidation of
1045 Atmospheric Organic Aerosol: Kinetics of Changes to the Amount and Oxidation State of
1046 Particle-Phase Organic Carbon, J. Phys. Chem. A, 119, 10767-10783,
1047 https://doi.org/10.1021/acs.jpca.5b06946, 2015.

1048 Kumar, N. K., Corbin, J. C., Bruns, E. A., Massabó, D., Slowik, J. G., Drinovec, L., Močnik, G.,
1049 Prati, P., Vlachou, A., Baltensperger, U., Gysel, M., El-Haddad, I., and Prévôt, A. S. H.:
1050 Production of particulate brown carbon during atmospheric aging of wood-burning emissions,
1051 Atmos. Chem. Phys., 2018, 17,843-817,861, https://doi.org/10.5194/acp-18-17843-2018, 2018.

1052 Lack, D. A., Langridge, J., Bahreni, R., Cappa, C. D., Middlebrook, A., and Schwarz, J. P.:
1053 Brown Carbon and Internal Mixing in Biomass Burning Particles, PNAS, 10, 14802-14807,
1054 https://doi.org/10.1073/pnas.1206575109, 2012.

1055 Lambe, A. T., Cappa, C. D., Massoli, P., Onasch, T. B., Forestieri, S. D., Martin, A. T.,
1056 Cummings, M. J., Croasdale, D. R., Brune, W. H., Worsnop, D. R., and Davidovits, P.:
1057 Relationship between Oxidation Level and Optical Properties of Secondary Organic Aerosol,
1058 Environmental Science & Technology, 47, 6349-6357, https://doi.org/10.1021/es401043j, 2013.

1059 Laskin, A., Laskin, J., and Nizkorodov, S. A.: Chemistry of Atmospheric Brown Carbon,
1060 Chemical Reviews, 115, 4335-4382, https://doi.org/10.1021/cr5006167, 2015.

1061 Lauraguais, A., Coeur-Tourneur, C., Cassez, A., Deboudt, K., Fourmentin, M., and Choël, M.:
1062 Atmospheric reactivity of hydroxyl radicals with guaiacol (2-methoxyphenol), a biomass burning
1063 emitted compound: Secondary organic aerosol formation and gas-phase oxidation products,
1064 Atmospheric Environment, 86, 155-163, https://doi.org/10.1016/j.atmosenv.2013.11.074, 2014.

1065 Lee, H. J., Aiona, P. K., Laskin, A., Laskin, J., and Nizkorodov, S. A.: Effect of Solar Radiation
1066 on the Optical Properties and Molecular Composition of Laboratory Proxies of Atmospheric
1067 Brown Carbon, Environmental Science & Technology, 48, 10217-10226,
1068 https://doi.org/10.1021/es502515r, 2014.

1069 Lelieveld, J., Evans, J. S., Fnais, M., Giannadaki, D., and Pozzer, A.: The contribution of outdoor
1070 air pollution sources to premature mortality on a global scale, Nature, 525, 367,
1071 https://doi.org/10.1038/nature15371, 2015.

1072 Levin, E. J. T., McMeeking, G. R., Carrico, C. M., Mack, L. E., Kreidenweis, S. M., Wold, C.
1073 E., Moosmüller, H., Arnott, W. P., Hao, W. M., Collett, J. L., and Malm, W. C.: Biomass
1074 burning smoke aerosol properties measured during Fire Laboratory at Missoula Experiments
1075 (FLAME), Journal of Geophysical Research: Atmospheres, 115, D18210,
1076 https://doi.org/10.1029/2009JD013601, 2010.

1077   Lewis, K., Arnott, W. P., Moosmüller, H., and Wold, C. E.: Strong spectral variation of biomass
1078   smoke light absorption and single scattering albedo observed with a novel dual-wavelength
1079   photoacoustic instrument, Journal of Geophysical Research: Atmospheres, 113, D16203,
1080   https://doi.org/10.1029/2007JD009699, 2008.

1081   Lim, C. Y., Hagan, D. H., Coggon, M. M., Koss, A. R., Sekimoto, K., De Gouw, J., Warneke,
1082   C., Cappa, C. D., and Kroll, J. H.: Secondary organic aerosol formation from biomass burning
1083   emissions, Atmos. Chem. Phys. Discuss., https://doi.org/10.5194/acp-2019-326, 2019.

1084   Liu, D. T., Whitehead, J., Alfarra, M. R., Reyes-Villegas, E., Spracklen, D. V., Reddington, C.
1085   L., Kong, S. F., Williams, P. I., Ting, Y. C., Haslett, S., Taylor, J. W., Flynn, M. J., Morgan, W.
1086   T., McFiggans, G., Coe, H., and Allan, J. D.: Black-carbon absorption enhancement in the
1087   atmosphere determined by particle mixing state, Nat. Geosci., 10, 184-U132,
1088   https://doi.org/10.1038/ngeo2901, 2017.

1089   Martinsson, J., Eriksson, A. C., Nielsen, I. E., Malmborg, V. B., Ahlberg, E., Andersen, C.,
1090   Lindgren, R., Nyström, R., Nordin, E. Z., Brune, W. H., Svenningsson, B., Swietlicki, E.,
1091   Boman, C., and Pagels, J. H.: Impacts of Combustion Conditions and Photochemical Processing
1092   on the Light Absorption of Biomass Combustion Aerosol, Environmental Science &
1093   Technology, 49, 14663-14671, https://doi.org/10.1021/acs.est.5b03205, 2015.

1094   McClure, C. D., and Jaffe, D. A.: US particulate matter air quality improves except in wildfire-
1095   prone areas, Proceedings of the National Academy of Sciences, 115, 7901-7906,
1096   https://doi.org/10.1073/pnas.1804353115, 2018.

1097   McClure, C. D., Lim, C. Y., Hagan, D. H., Kroll, J. H., and Cappa, C. D.: Biomass-burning
1098   derived particles from a wide variety of fuels: Part 1: Properties of primary particles, Atmos.
1099   Chem. Phys. Discuss., 2019, 1-37, https://doi.org/10.5194/acp-2019-707, 2019.

1100   McMeeking, G. R., Kreidenweis, S. M., Baker, S., Carrico, C. M., Chow, J. C., Collett, J. L.,
1101   Hao, W. M., Holden, A. S., Kirchstetter, T. W., Malm, W. C., Moosmüller, H., Sullivan, A. P.,
1102   and Wold, C. E.: Emissions of trace gases and aerosols during the open combustion of biomass
1103   in the laboratory, Journal of Geophysical Research: Atmospheres, 114, D19210,
1104   https://doi.org/10.1029/2009JD011836, 2009.

1105   Metcalf, A. R., Loza, C. L., Coggon, M. M., Craven, J. S., Jonsson, H. H., Flagan, R. C., and
1106   Seinfeld, J. H.: Secondary Organic Aerosol Coating Formation and Evaporation: Chamber
1107   Studies Using Black Carbon Seed Aerosol and the Single-Particle Soot Photometer, Aerosol Sci.
1108   Technol., 47, 326-347, https://doi.org/10.1080/02786826.2012.750712, 2013.

1109   NOAA: Fire Influence on Regional to Global Environments and Air Quality (FIREX-AQ),
1110   https://www.esrl.noaa.gov/csd/projects/firex-aq/whitepaper.pdf, 2013.

1111   Orlando, J. J., and Tyndall, G. S.: Laboratory studies of organic peroxy radical chemistry: an
1112   overview with emphasis on recent issues of atmospheric significance, Chemical Society
1113   Reviews, 41, 6294-6317, https://doi.org/10.1039/c2cs35166h, 2012.

1114   Peng, J., Hu, M., Guo, S., Du, Z., Zheng, J., Shang, D., Zamora, M. L., Zeng, L., Shao, M., Wu,
1115   Y.-S., Zheng, J., Wang, Y., Glen, C. R., Collins, D. R., Molina, M. J., and Zhang, R.: Markedly
1116   enhanced absorption and direct radiative forcing of black carbon under polluted urban
1117   environments, Proc. Natl. Acad. Sci. U. S. A., 113, 4266-4271,
1118   https://doi.org/10.1073/pnas.1602310113, 2016a.

1119 Peng, Z., Day, D. A., Ortega, A. M., Palm, B. B., Hu, W., Stark, H., Li, R., Tsigaridis, K., Brune,
1120 W. H., and Jimenez, J. L.: Non-OH chemistry in oxidation flow reactors for the study of
1121 atmospheric chemistry systematically examined by modeling, Atmos. Chem. Phys., 16, 4283-
1122 4305, https://doi.org/10.5194/acp-16-4283-2016, 2016b.

1123 Penner, J. E., Dickinson, R. E., and O'Neill, C. A.: Effects of Aerosol from Biomass Burning on
1124 the Global Radiation Budget, Science, 256, 1432-1434,
1125 https://doi.org/10.1126/science.256.5062.1432, 1992.

1126 Richards-Henderson, N. K., Goldstein, A. H., and Wilson, K. R.: Sulfur Dioxide Accelerates the
1127 Heterogeneous Oxidation Rate of Organic Aerosol by Hydroxyl Radicals, Environmental
1128 Science & Technology, 50, 3554-3561, https://doi.org/10.1021/acs.est.5b05369, 2016.

1129 Romonosky, D. E., Ali, N. N., Saiduddin, M. N., Wu, M., Lee, H. J., Aiona, P. K., and
1130 Nizkorodov, S. A.: Effective absorption cross sections and photolysis rates of anthropogenic and
1131 biogenic secondary organic aerosols, Atmospheric Environment, 130, 172-179,
1132 https://doi.org/10.1016/j.atmosenv.2015.10.019, 2016.

1133 Saleh, R., Hennigan, C. J., McMeeking, G. R., Chuang, W. K., Robinson, E. S., Coe, H.,
1134 Donahue, N. M., and Robinson, A. L.: Absorptivity of brown carbon in fresh and photo-
1135 chemically aged biomass-burning emissions, Atmospheric Chemistry and Physics, 13, 7683-
1136 7693, https://doi.org/10.5194/acp-13-7683-2013, 2013.

1137 Saleh, R., Robinson, E. S., Tkacik, D. S., Ahern, A. T., Liu, S., Aiken, A. C., Sullivan, R. C.,
1138 Presto, A. A., Dubey, M. K., Yokelson, R. J., Donahue, N. M., and Robinson, A. L.: Brownness
1139 of organics in aerosols from biomass burning linked to their black carbon content, Nature
1140 Geosci, 7, 647-650, https://doi.org/10.1038/ngeo2220, 2014.

1141 Schnitzler, E. G., and Abbatt, J. P. D.: Heterogeneous OH oxidation of secondary brown carbon
1142 aerosol, Atmospheric Chemistry and Physics, 18, 14539-14553, https://doi.org/10.5194/acp-18-
1143 14539-2018, 2018.

1144 Sekimoto, K., Koss, A. R., Gilman, J. B., Selimovic, V., Coggon, M. M., Zarzana, K. J., Yuan,
1145 B., Lerner, B. M., Brown, S. S., Warneke, C., Yokelson, R. J., Roberts, J. M., and de Gouw, J.:
1146 High- and low-temperature pyrolysis profiles describe volatile organic compound emissions
1147 from western US wildfire fuels, Atmos. Chem. Phys., 18, 9263-9281,
1148 https://doi.org/10.5194/acp-18-9263-2018, 2018.

1149 Selimovic, V., Yokelson, R. J., Warneke, C., Roberts, J. M., de Gouw, J., Reardon, J., and
1150 Griffith, D. W. T.: Aerosol optical properties and trace gas emissions by PAX and OP-FTIR for
1151 laboratory-simulated western US wildfires during FIREX, Atmos. Chem. Phys., 18, 2929-2948,
1152 https://doi.org/10.5194/acp-18-2929-2018, 2018.

1153 Sherwood, S.: A Microphysical Connection Among Biomass Burning, Cumulus Clouds, and
1154 Stratospheric Moisture, Science, 295, 1272-1275, https://doi.org/10.1126/science.1065080, 2002.

1155 Shiraiwa, M., Kondo, Y., Iwamoto, T., and Kita, K.: Amplification of Light Absorption of Black
1156 Carbon by Organic Coating, Aerosol Science and Technology, 44, 46-54,
1157 https://doi.org/10.1080/02786820903357686, 2010.

1158 Smith, J. D., Kroll, J. H., Cappa, C. D., Che, D. L., Liu, C. L., Ahmed, M., Leone, S. R.,
1159 Worsnop, D. R., and Wilson, K. R.: The heterogeneous reaction of hydroxyl radicals with sub-

Atmospheric
Chemistry
and Physics
Discussions

1160   micron squalane particles: a model system for understanding the oxidative aging of ambient
1161   aerosols, Atmos. Chem. Phys., 9, 3209-3222, https://doi.org/10.5194/acp-9-3209-2009, 2009.

1162   Stephens, S. L., Agee, J. K., Fulé, P. Z., North, M. P., Romme, W. H., Swetnam, T. W., and
1163   Turner, M. G.: Managing Forests and Fire in Changing Climates, Science, 342, 41-42,
1164   https://doi.org/10.1126/science.1240294, 2013.

1165   Sumlin, B. J., Pandey, A., Walker, M. J., Pattison, R. S., Williams, B. J., and Chakrabarty, R. K.:
1166   Atmospheric Photooxidation Diminishes Light Absorption by Primary Brown Carbon Aerosol
1167   from Biomass Burning, Environmental Science & Technology Letters, 4, 540-545,
1168   https://doi.org/10.1021/acs.estlett.7b00393, 2017.

1169   Sun, Y. H., Xu, F., Li, X. F., Zhang, Q. Z., and Gu, Y. X.: Mechanisms and kinetic studies of
1170   OH-initiated atmospheric oxidation of methoxyphenols in the presence of O-2 and NOx,
1171   Physical Chemistry Chemical Physics, 21, 21856-21866, https://doi.org/10.1039/c9cp03246k,
1172   2019.

1173   Tasoglou, A., Saliba, G., Subramanian, R., and Pandis, S. N.: Absorption of chemically aged
1174   biomass burning carbonaceous aerosol, J Aerosol Sci, 113, 141-152,
1175   https://doi.org/10.1016/j.jaerosci.2017.07.011, 2017.

1176   Tritscher, T., Dommen, J., DeCarlo, P. F., Gysel, M., Barmet, P. B., Praplan, A. P., Weingartner,
1177   E., Prévôt, A. S. H., Riipinen, I., Donahue, N. M., and Baltensperger, U.: Volatility and
1178   hygroscopicity of aging secondary organic aerosol in a smog chamber, Atmos. Chem. Phys., 11,
1179   11477-11496, https://doi.org/10.5194/acp-11-11477-2011, 2011.

1180   Vakkari, V., Kerminen, V.-M., Beukes, J. P., Tiitta, P., Zyl, P. G., Josipovic, M., Venter, A. D.,
1181   Jaars, K., Worsnop, D. R., Kulmala, M., and Laakso, L.: Rapid changes in biomass burning
1182   aerosols by atmospheric oxidation, Geophysical Research Letters, 41, 2644-2651,
1183   https://doi.org/doi:10.1002/2014GL059396, 2014.

1184   Vereecken, L.: Reaction Mechanisms for the Atmospheric Oxidation of Monocyclic Aromatic
1185   Compounds, in: Advances in Atmospheric Chemistry, edited by: Barker, J. R., Steiner, A. L.,
1186   and Wallington, T. J., World Scientific, 377-527, 2019.

1187   Wang, X., Heald, C. L., Ridley, D. A., Schwarz, J. P., Spackman, J. R., Perring, A. E., Coe, H.,
1188   Liu, D., and Clarke, A. D.: Exploiting simultaneous observational constraints on mass and
1189   absorption to estimate the global direct radiative forcing of black carbon and brown carbon,
1190   Atmospheric Chemistry and Physics, 14, 10989-11010, https://doi.org/10.5194/acp-14-10989-
1191   2014, 2014.

1192   Wang, X., Heald, C. L., Sedlacek, A. J., de Sá, S. S., Martin, S. T., Alexander, M. L., Watson, T.
1193   B., Aiken, A. C., Springston, S. R., and Artaxo, P.: Deriving brown carbon from
1194   multiwavelength absorption measurements: method and application to AERONET and
1195   Aethalometer observations, Atmos. Chem. Phys., 16, 12733-12752, https://doi.org/10.5194/acp-
1196   16-12733-2016, 2016.

1197   Wang, X., Heald, C. L., Liu, J., Weber, R. J., Campuzano-Jost, P., Jimenez, J. L., Schwarz, J. P.,
1198   and Perring, A. E.: Exploring the observational constraints on the simulation of brown carbon,
1199   Atmos. Chem. Phys., 18, 635-653, https://doi.org/10.5194/acp-18-635-2018, 2018.

Atmospheric
Chemistry
and Physics
Discussions

1200 Wong, J. P. S., Nenes, A., and Weber, R. J.: Changes in Light Absorptivity of Molecular Weight
1201 Separated Brown Carbon Due to Photolytic Aging, Environmental Science & Technology, 51,
1202 8414-8421, https://doi.org/10.1021/acs.est.7b01739, 2017.

1203 Xie, M., Chen, X., Hays, M. D., Lewandowski, M., Offenberg, J., Kleindienst, T. E., and Holder,
1204 A. L.: Light Absorption of Secondary Organic Aerosol: Composition and Contribution of
1205 Nitroaromatic Compounds, Environmental Science & Technology, 51, 11607-11616,
1206 https://doi.org/10.1021/acs.est.7b03263, 2017.

1207 You, R., Radney, J. G., Zachariah, M. R., and Zangmeister, C. D.: Measured Wavelength-
1208 Dependent Absorption Enhancement of Internally Mixed Black Carbon with Absorbing and
1209 Nonabsorbing Materials, Environmental Science & Technology, 50, 7982-7990,
1210 https://doi.org/10.1021/acs.est.6b01473, 2016.

1211 Yuan, B., Koss, A. R., Warneke, C., Coggon, M., Sekimoto, K., and de Gouw, J. A.: Proton-
1212 Transfer-Reaction Mass Spectrometry: Applications in Atmospheric Sciences, Chemical
1213 Reviews, 117, 13187-13229, https://doi.org/10.1021/acs.chemrev.7b00325, 2017.

1214 Zhang, X., Cappa, C. D., Jathar, S. H., McVay, R. C., Ensberg, J. J., Kleeman, M. J., and
1215 Seinfeld, J. H.: Influence of vapor wall loss in laboratory chambers on yields of secondary
1216 organic aerosol, Proceedings of the National Academy of Sciences, 111, 5802-5807,
1217 https://doi.org/10.1073/pnas.1404727111, 2014.

1218 Zhang, Y., Forrister, H., Liu, J., Dibb, J., Anderson, B., Schwarz, J. P., Perring, A. E., Jimenez, J.
1219 L., Campuzano-Jost, P., Wang, Y., Nenes, A., and Weber, R. J.: Top-of-atmosphere radiative
1220 forcing affected by brown carbon in the upper troposphere, Nat. Geosci., 10, 486,
1221 https://doi.org/10.1038/ngeo2960, 2017.

1222 Zhong, M., and Jang, M.: Dynamic light absorption of biomass-burning organic carbon
1223 photochemically aged under natural sunlight, Atmos. Chem. Phys., 14, 1517-1525,
1224 https://doi.org/10.5194/acp-14-1517-2014, 2014a.

1225 Zhong, M., and Jang, M.: Dynamic light absorption of biomass-burning organic carbon
1226 photochemically aged under natural sunlight, Atmospheric Chemistry and Physics, 14, 1517-
1227 1525, https://doi.org/10.5194/acp-14-1517-2014, 2014b.

1228

1229

1230   **10 Tables**

1231   **Table 1.** Model parameters for NMOG

Property	Fast	Slow	Very Slow	Multi Generation	Heterogeneous
$MAC_{BrC,405nm}$[**]	0.81	0.05	0.05	0.17	0.05
α[**]	0.43	0.13	0.05	0.45	--
k_{OH} (cm^3 $molecules^{-1}$ s^{-1})	4×10^{-11}	9×10^{-12}	7×10^{-13}	5×10^{-12}	--
γ_{OH}	--	--	--	--	1
O:C[^,***]	0.73	0.59	0.59[&]	+1.22[#]	+1.22[#]
AMS f_{60}[***]	0.008	0.003	0.003[&]	0.006	0.008,0.003,0.01[*]

-- = not applicable

[^] It is assumed that the carbon backbone has 8 carbon atoms. The assumed O:C values therefore correspond to 5.8, 4.7, and 4.7 oxygen atoms per molecule for the fast, slow and very slow SOA.

[&] Assumed to equal the slow SOA

[#] It is assumed that every reaction leads to addition n oxygen atoms, where n is the indicated value. Consequently, the average O:C for multi-generation products increases over time as the multi-generation species accumulate oxygen.

[*] Values for oxidation products from internally mixed POA, externally mixed POA, and SOA.

[**] Determined from global fit to the $MAC_{BrC,405nm}$ and [OA]/[rBC] observations.

[***] Determined from a global fit to the O:C or f_{60} observations after determining the α values.

1232

1233

Atmospheric
Chemistry
and Physics
Discussions

1234   **Table 2.** Model parameters by particle class

Property	class 1	class 2	class 3	class 4	class 5	class 6
[NMOG]:[POA][*,^]	2.8	4.4	3.8	6.3	5.6	6.2
[POA]/[BC][#,*]	1.3	3.5	12	24	85	12,000
$MAC_{BrC,405nm, POA}$[#]	2.5	1.2	0.73	0.66	0.57	0.39
$O:C_{POA}$[#]	0.45	0.35	0.40	0.42	0.37	0.2
Fraction internally mixed[#]	0.90	0.32	0.14	0.12	0.09	0.01
AMS $f_{60,POA}$[#]	0.015	0.019	0.021	0.025	0.021	0.0124
$F_{NMOG,fast}$[^]	0.20	0.36	0.27	0.47	0.53	0.42
$F_{NMOG,slow}$[^]	0.70	0.54	0.63	0.43	0.37	0.48
$F_{NMOG,VS}$[+]	0.1	0.1	0.1	0.1	0.1	0.1

[#] Directly constrained from observations
[*] Mass ratio (unitless); [+] units = $m^2 \, g^{-1}$
[^] Determined from a global fit to the $MAC_{BrC,405nm}$ and [OA]/[rBC]
[+] Specified as a constant

1235

1236

1237

1238

1239

1240

1241 **11 Figures**
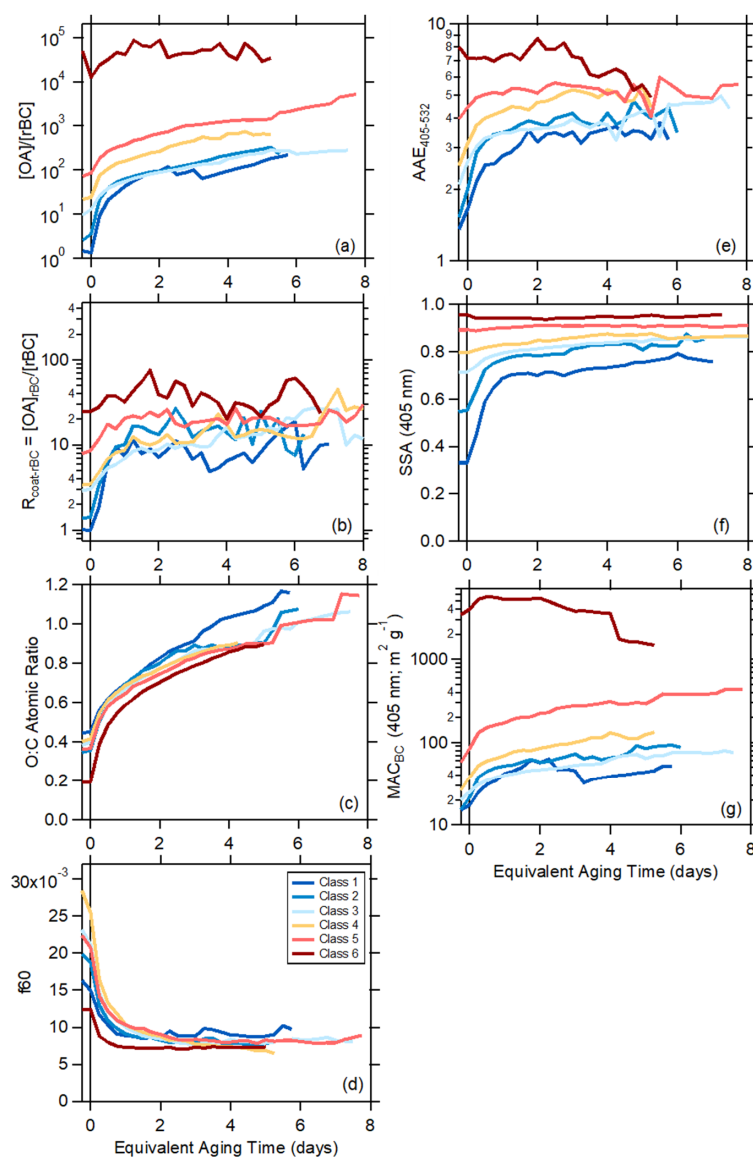
1242

1243 **Figure 1.** Relationship between (a) the [OA]/[rBC] ratio, (b) $R_{coat-rBC}$, (c) $AAE_{405-532}$, (d) the SSA

1244 at 405 nm, (e) the O:C atomic ratio, and (f) the AMS f_{60}, as a function of equivalent photochemical

1245 aging time (assuming [OH] = 1.5 x 10^6 molecules cm^{-3}). The different lines are colored according

1246 to the SSA classification, and are averages for all burns within a class (see Panel D). Figures

1247 showing results for each burn are available in the Supplementary Material. Some of the apparent

1248 discontinuities for individual classes with certain properties results from a change in the number

1249 of individual experiments contributing to the average above a given aging time.

1250
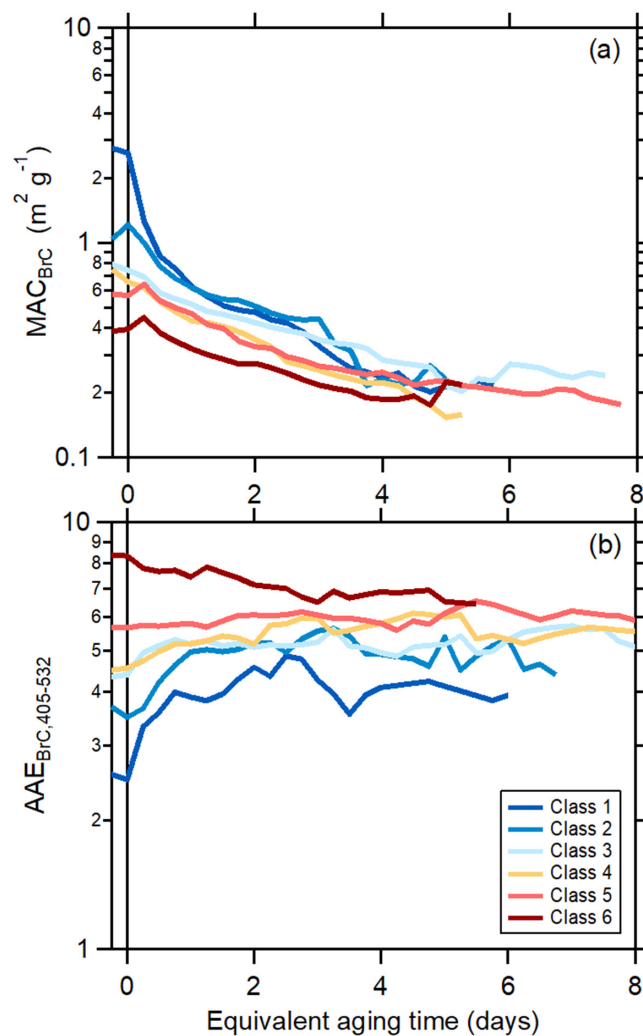
1251

Figure 2. Relationship between the brown carbon (a) MAC_{BrC} and (b) the AAE_{BrC} as a function of equivalent photochemical aging time (assuming $[OH] = 1.5 \times 10^6$ molecules cm^{-3}). The different lines are colored according to the SSA classification, and are averages for all burns within a class. class 1 corresponds to particles having low SSA_{405} and class 6 to particles having high SSA_{405}nm. Figures showing results for each burn are available in the Supplementary Material.

1257

1258
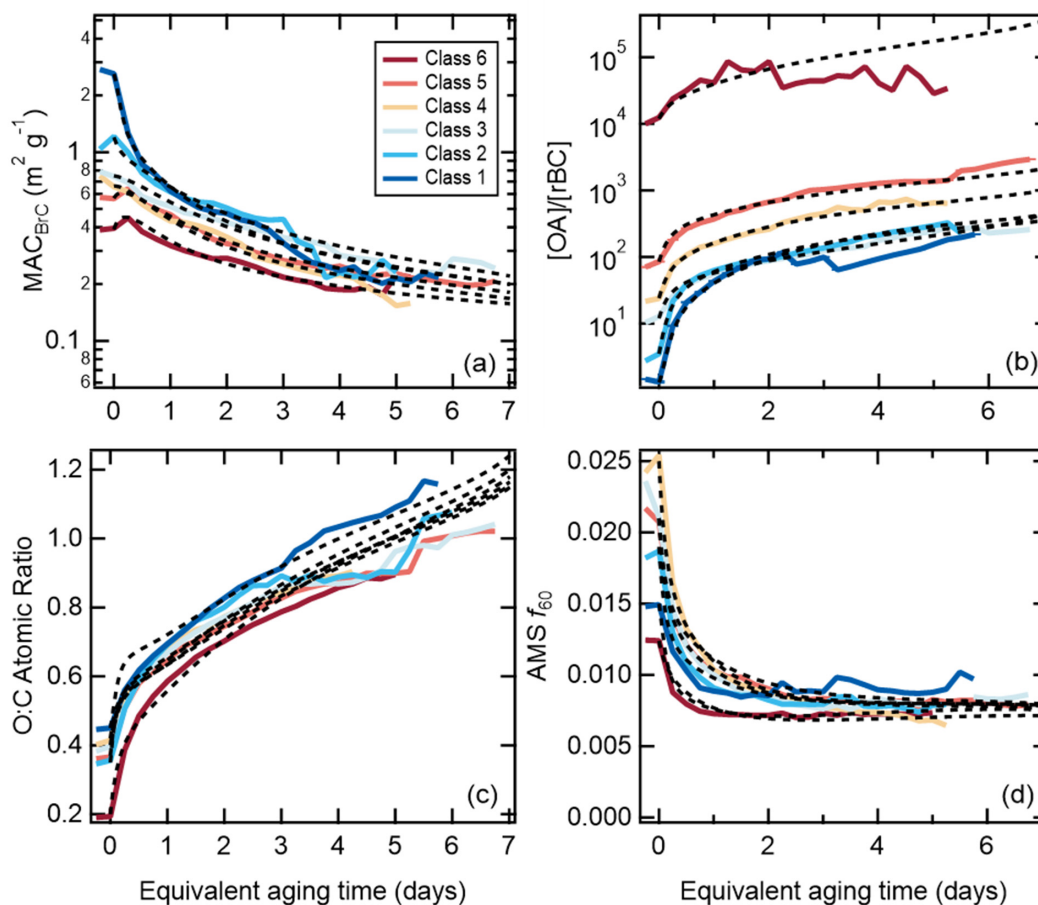
1259
1260 **Figure 3.** Comparison between observed (solid lines) and modeled (dashed lines) values of the
1261 (a) MAC_{BrC}, (b) the [OA]/[rBC] ratio, (c) the O:C atomic ratio, and (d) the AMS f_{60} and the
1262 equivalent photochemical aging time (assuming [OH] = 1.5 x 10^6 molecules cm^{-3}), with results
1263 shown for each SSA class.
1264

1265
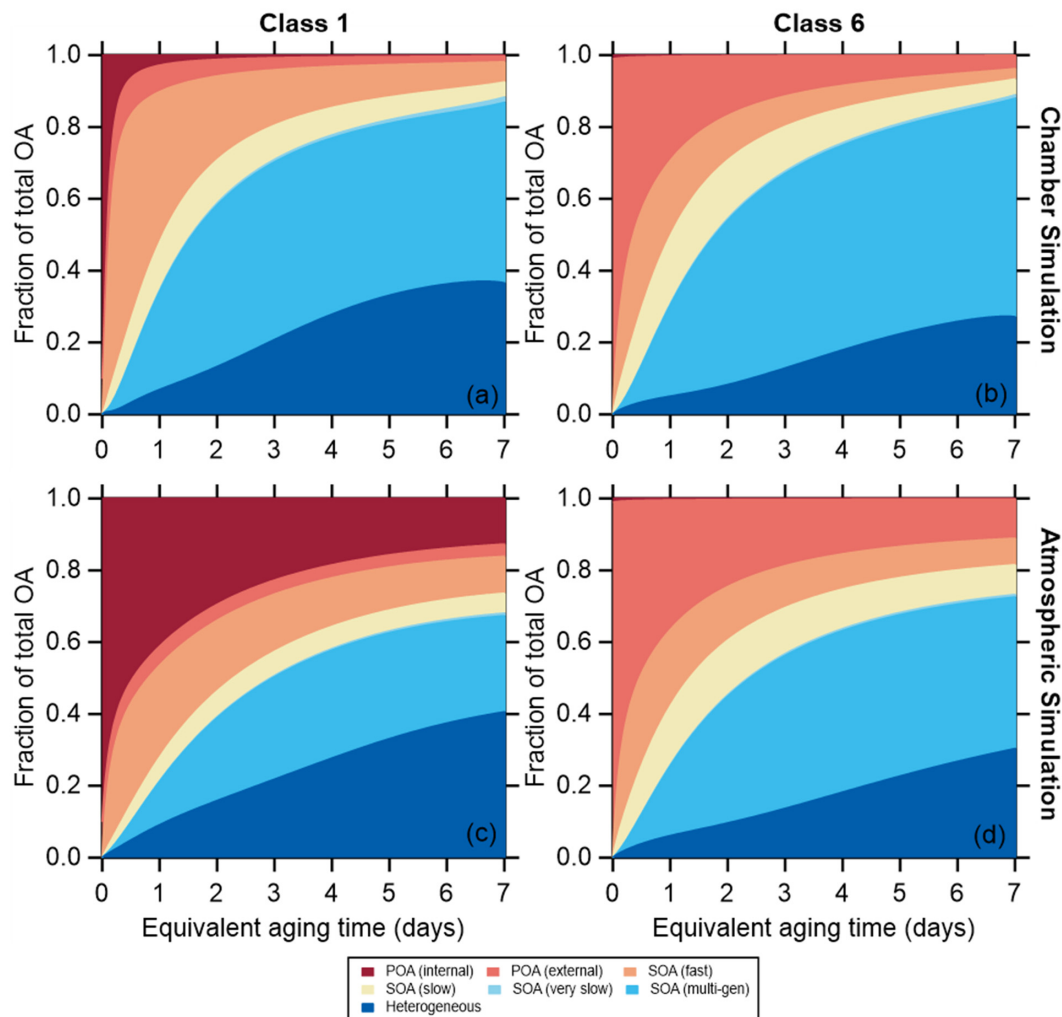
1266
1267 **Figure 4.** Variation in the simulated OA fractional composition with equivalent aging time for (a
1268 and c) SSA class 1 (BC rich) and (b and d) SSA class 6 (OA rich) for the mini chamber
1269 experiments. For the "chamber" simulations in (a and b) the differences in decay rates between
1270 particle types and gases are accounted for. For the "atmospheric" simulations in (c and d) it is
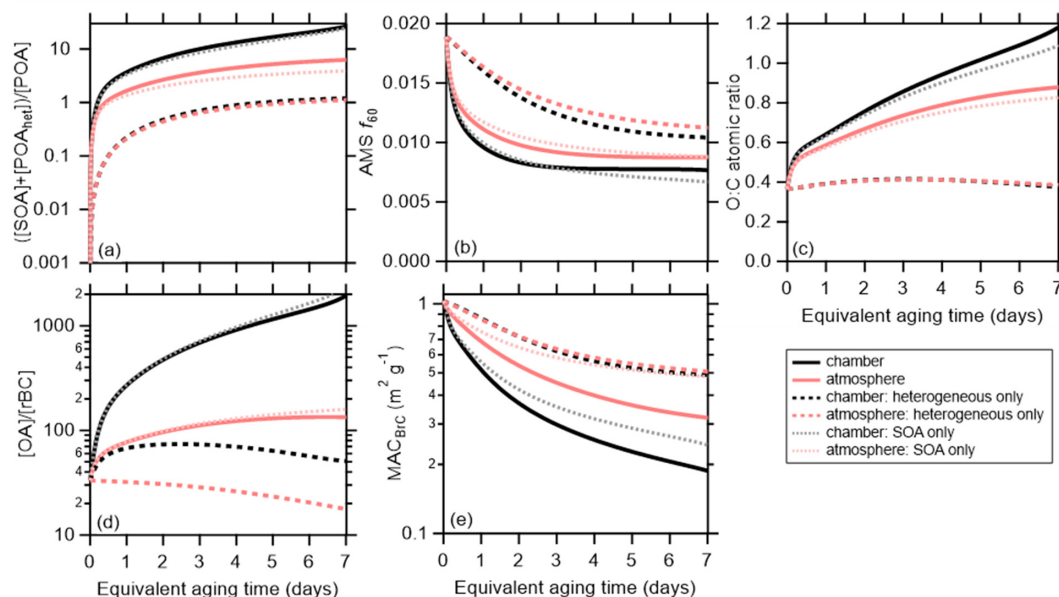1271 assumed that gases and particles all decay with the same rate.
1272

1273
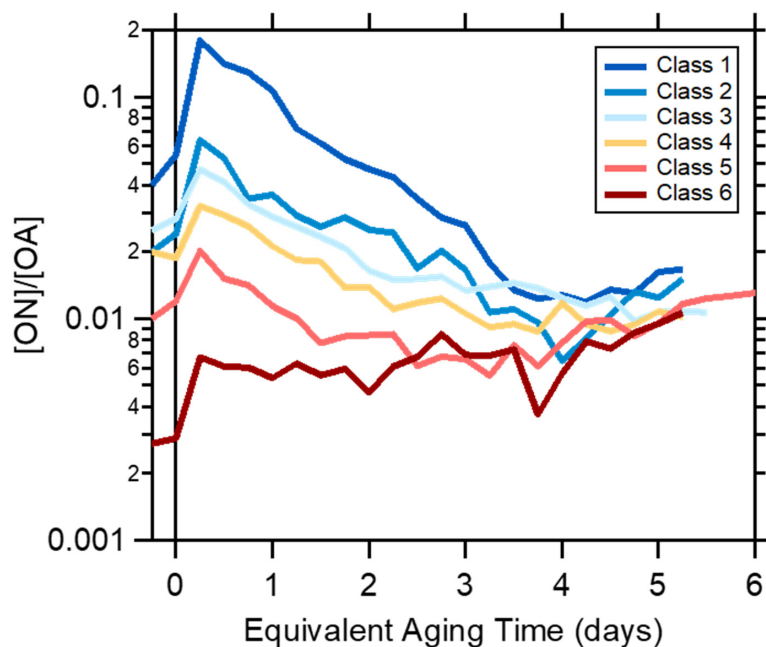
Figure 5. Dependence of the observed organic nitrate-to-total OA ratio for each SSA class on the equivalent aging time (assuming $[OH] = 1.5 \times 10^6$ molecules cm^{-3}).
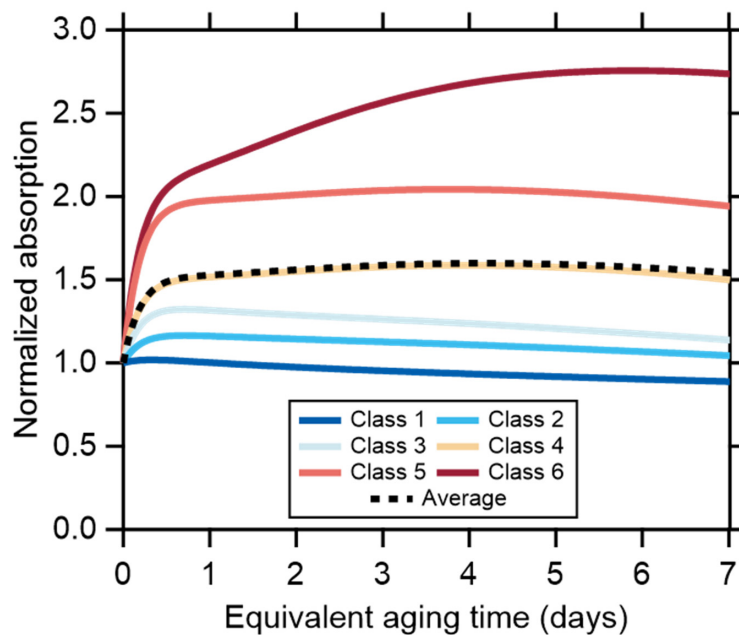
1279

1280
1281
1282 **Figure 6.** Comparison between the model results when dilution and wall-losses are included (the
1283 chamber simulation, black lines) or turned off (the atmospheric simulation, red lines). The model
1284 has been run with both SOA formation and heterogeneous oxidation (solid lines), with
1285 heterogeneous oxidation only (dashed lines), or with SOA formation only (dotted lines).
1286 Averages (either arithmetic or geometric) across all particle classes are shown for (a) the SOA
1287 plus oxidized POA to unoxidized POA ratio, (b) the AMS f_{60}, (c) the organic O:C, (d) the OA-to-
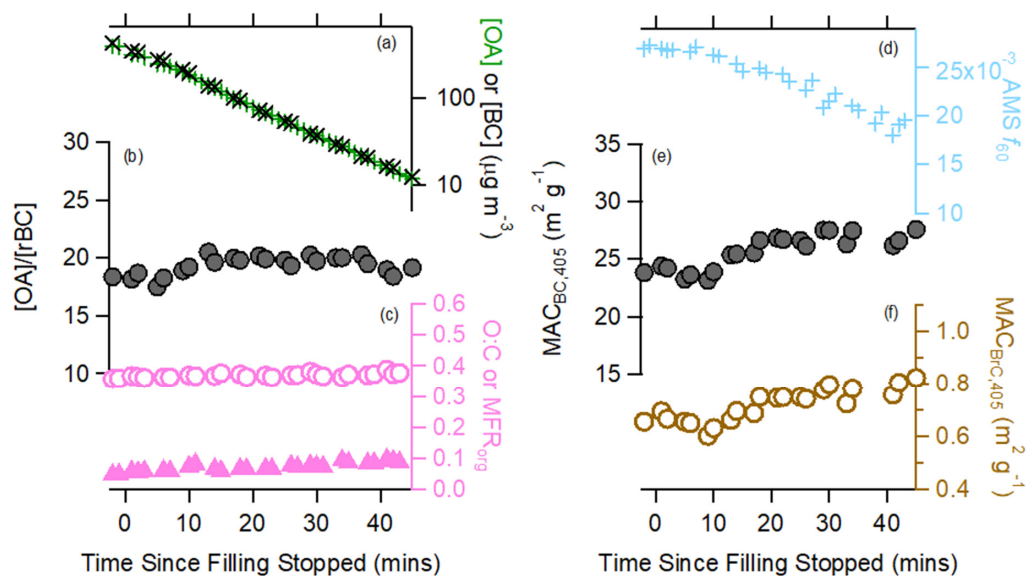1288 rBC ratio, and (e) the $MAC_{BrC,405}$.
1289
1290

Atmospheric
Chemistry
and Physics
Discussions
Open Access
EGU

1291
1292
1293

1294
1295
1296 **Figure 7.** Modeled change in the absolute absorption with aging, assuming no dilution,
1297 normalized to the value at $t = 0$. Results are shown for each particle class (colors) and the
1298 average (black).
1299
1300

Figure 8. Variation in various particle properties with time during the dark experiment. The change in (a) either the [OA] (green) or [rBC] (black), with [rBC] multiplied by 20; (b) the [OA]/[rBC] ratio; (c) the O:C ratio (circles) or OA mass fraction remaining (triangles); (d) the AMS f_{60} biomass burning marker; (e) the $MAC_{BC,405nm}$; and (f) the $MAC_{BrC,405nm}$.